














Atacama Compact Array Measurements of the Molecular Mass in the NGC 5044 Cooling-flow Group

Gerrit Schellenberger¹ , Laurence P. David¹, Jan Vrtilek¹, Ewan O’Sullivan¹ , Jeremy Lim², William Forman¹ , Ming Sun³ , Françoise Combes⁴ , Philippe Salomé⁴, Christine Jones¹, Simona Giacintucci⁵ , Alastair Edge⁶ , Fabio Gastaldello⁷ , Pasquale Temi⁸ , Fabrizio Brighenti⁹ , and Sandro Bardelli¹⁰ 

¹ Center for Astrophysics | Harvard & Smithsonian, 60 Garden Street, Cambridge, MA 02138, USA; gerrit.schellenberger@cfa.harvard.edu

² Department of Physics, University of Hong Kong, Pokfulam Road, Hong Kong, People’s Republic of China

³ Department of Physics, University of Alabama in Huntsville, Huntsville, AL 35899, USA

⁴ Observatoire de Paris, LERMA, CNRS, 61 Avenue de l’Observatoire, F-75014 Paris, France

⁵ Naval Research Laboratory, 4555 Overlook Avenue SW, Code 7213, Washington, DC 20375, USA

⁶ Institute for Computational Cosmology, Department of Physics, Durham University, South Road, Durham DH1 3LE, UK

⁷ INAF—IASF-Milano, Via E. Bassini 15, I-20133 Milano, Italy

⁸ Astrophysics Branch, NASA/Ames Research Center, MS 245-6, Moffett Field, CA 94035, USA

⁹ Dipartimento di Astronomia, Università di Bologna, via Ranzani 1, I-40127 Bologna, Italy

¹⁰ INAF—Astrophysics and Space Science Observatory Bologna, via Gobetti 93/3, I-40129 Bologna, Italy

Received 2019 September 12; revised 2020 March 26; accepted 2020 April 6; published 2020 May 7

Abstract

The fate of cooling gas in the centers of galaxy clusters and groups is still not well understood, as is also the case for the complex processes of triggering star formation in central dominant galaxies, reheating of cooled gas by active galactic nuclei (AGN), and the triggering or “feeding” of supermassive black hole outbursts. We present CO observations of the early-type galaxy NGC 5044, which resides at the center of an X-ray bright group with a moderate cooling flow. For our analysis we combine CO(2–1) data from the 7 m antennae of the Atacama Compact Array (ACA) and the ACA total power array (TP). We demonstrate, using the 7 m array data, that we can recover the total flux inferred from IRAM 30 m single-dish observations, which corresponds to a total molecular mass of about $4 \times 10^7 M_\odot$. Most of the recovered flux is blueshifted with respect to the galaxy rest frame and is extended on kiloparsec-scales, suggesting low filling factor dispersed clouds. We find eight concentrations of molecular gas out to a radius of $10''$ (1.5 kpc), which we identify with giant molecular clouds. The total molecular gas mass is more centrally concentrated than the X-ray emitting gas, but is extended in the northeast-southwest direction beyond the IRAM 30 m beam. We also compare the spatial extent of the molecular gas to the H α emission: The CO emission coincides with the very bright H α region in the center. We do not detect CO emission in the fainter H α regions. Furthermore, we find two CO absorption features spatially located at the center of the galaxy, within 5 pc projected distance of the AGN, infalling at 255 and 265 km s^{−1} relative to the AGN. This indicates that the two giant molecular clouds seen in absorption are most likely within the sphere of influence of the supermassive black hole.

Unified Astronomy Thesaurus concepts: Galaxy clusters (584); Early-type galaxies (429); Active galactic nuclei (16); Giant molecular clouds (653); Cooling flows (2028); Molecular gas (1073)

1. Introduction

The increasing density of hot X-ray emitting gas toward the centers of galaxy clusters and groups predicts short cooling times, resulting in large amounts of cold gas (e.g., Fabian 1994; Salomé & Combes 2003; David et al. 2014). Simulations also show that the densest parts of the H α filaments can cool to molecular clouds with masses of several $1 \times 10^7 M_\odot$ (Gaspari et al. 2017). Active galactic nuclei (AGN) have been found to be a significant reheating source, and may resolve the conflict between higher apparent cooling rates and minimal star formation in X-ray luminous groups and clusters. Cold molecular gas has been found to form in the central dominant galaxies (CDGs) of several systems (e.g., Edge 2001; Salomé & Combes 2003, and more recently, Tremblay et al. 2016; Vantyghem et al. 2017; O’Sullivan et al. 2018; Rose et al. 2019b). In these studies, single-dish CO measurements have turned out to be essential to reveal the total molecular gas resulting from cooling in the centers of groups and clusters (McNamara & Nulsen 2007; Russell et al. 2014; McNamara et al. 2016; Russell et al. 2016, 2017a, 2017b). However, in

order to make a comparison to feedback models, a more precise location of these cold-gas reservoirs is needed: Are they associated in small or large clouds, or fully diffuse? High-resolution interferometry measurements (e.g., with the Atacama Large Millimeter/submillimeter Array, ALMA) have found small (with respect to the total CO flux) clouds of CO (David et al. 2014; Temi et al. 2018; Olivares et al. 2019). However, the integrated mass of these clouds is inconsistent with the single-dish measurements, indicating that the large baselines of ALMA are unable to capture a large fraction of the molecular gas (Olivares et al. 2019). ALMA alone cannot provide a comprehensive picture of the cold gas in clusters and groups. The Atacama Compact Array (ACA) with its shorter baselines closes the gap with single-dish measurements. The ACA is composed of 12 7 m antennae (7 m array) used in interferometry mode and 4 12 m antennae used in total power mode (TP array). The configuration of the ACA ensures superb coverage of short baselines, and a spatial resolution close to $5''$.

NGC 5044 is one of the X-ray brightest galaxy groups in the sky. The wealth of multifrequency data available for this object makes it an ideal candidate for studying the correlations of gas

Table 1
ALMA Observing Log

	12 m Cycle 0	12 m Cycle 4 Extended	7 m Cycle 4	12 m Cycle 4 Compact	Total Power
Date	2012 Jan 13	2017 Aug 3	2016 July	2016 Nov 15	2018 Oct–Dec
Project Code	2011.0.00735.S	2016.1.00533.S	2016.2.00134.S	2016.1.00533.S	2017.1.00784.S
Time (min)	29	44	306	48	614
Bandpass	3C273	J1337–1257	J1256–0547	J1337–1257	...
Phase	J1337–129	J1258–1800	J1337–1257	J1305–1033	...
Amplitude	Titan	Titan	Titan	Titan	...
Number of Ant	18	46	11	42	2–4
rms (mJy bm ⁻¹)	1.4	0.49	1.8	0.47	12
Beam size(" × ")	2.1 × 1.1	0.13 × 0.11	6.9 × 5.1	0.54 × 0.47	28.4 × 28.4
Beam size(pc × pc)	315 × 165	20 × 17	1050 × 765	81 × 70	4300 × 4300
Δv (km s ⁻¹)	0.64	1.48	0.59	1.48	1.48
Used here	flux comparison	absorption	flux and new clouds	not used	together with 7m

Note. Observation date, ALMA project code, on-target science integration time, calibrators, number of antennae, rms sensitivity for channel width 10 km s⁻¹, restoring beam, velocity resolution, and application in this paper. For the total power observations three calibrators for the water vapor radiometry were used: J1245–1616, J1337–1257, and J1305–1033.

properties over a broad range of temperatures. H α filaments, the [C II] line, and CO emission show that some gas must be cooling out of the hot phase (David et al. 2014; Werner et al. 2014). Prior studies using exceptionally deep high-resolution X-ray data have shown that the hot gas within the central region has been perturbed by at least three cycles of AGN outbursts (David et al. 2009; Giacintucci et al. 2011; David et al. 2017). David et al. (2014) have spatially resolved clumps of molecular gas from CO 2–1 line emission in the central early-type galaxy with ALMA. Furthermore, in NGC 5044 most of the emission that has been detected in single-dish observations with the IRAM 30 m telescope was missed by the early ALMA measurements, despite ALMA having lower noise levels and thus higher sensitivity. However, the ALMA observation misses the shortest baselines needed to recover the full flux. In order to understand the cooling processes in the centers of clusters and groups, one needs to have a full census of the giant molecular clouds, including their precise position in spatial and velocity space, to enable a useful comparison with competing models for the feedback process. This requires observations with interferometers in multiple array configurations to cover the different sizes and scales of molecular clouds. H α and [C II] λ 158 μ m observations (Werner et al. 2014) show that in the case of NGC 5044, the filaments of cooling gas extend out to 8 kpc, while multiphase gas in the X-rays has been detected out to 15 kpc (David et al. 2017). Cold-gas CO measurements confirm the existence of giant molecular clouds (David et al. 2014) in the central 2 kpc, with sizes below 800 pc. However, single-dish measurements show that most of the gas must be on larger scales.

Our early (cycle 0) ALMA observation of NGC 5044 has also been analyzed by Temi et al. (2018), who found results consistent with David et al. (2014) for the most significant clouds in terms of cloud location and size. Almost all central clouds and the clouds located northwest of the AGN are confirmed, while nine clouds, mostly in the east, are unconfirmed and two new clouds are detected. The physical properties of the confirmed clouds are in good agreement with David et al. (2014). To extend these measurements in terms of covered spatial scales, we present new ACA observations of the galaxy group NGC 5044.

In Section 2 we describe the ACA data products and processing. Section 3 presents our main results, including a comparison of the 7 m array spectrum with the IRAM 30 m spectrum, estimates of the total molecular mass in the system and on which scales the gas is distributed, the detection of clouds and a comparison to the David et al. (2014) findings, and the two absorption features in the spectrum. Section 4 gives a comparison of the detected molecular clouds with clouds detected in other systems and simulations, and discusses the virial equilibrium in these clouds. We also constrain the physical distance of the clouds seen in absorption, and the implication for AGN feedback. Our findings are summarized in Section 5.

In this paper we assume a flat Λ CDM cosmology with $H_0 = 70$ km s⁻¹ Mpc⁻¹, and $\Omega_m = 0.3$. We adopt a systemic velocity of 2757 km s⁻¹ (heliocentric) for NGC 5044 and a luminosity distance of 31.2 Mpc (Tonry et al. 2001), which gives a physical scale in the rest frame of NGC 5044 of 1" = 150 pc. Uncertainties are given at the 1 σ level throughout the paper.

2. ALMA Data Reduction

NGC 5044 was observed in cycle 4 with two different ALMA configurations (compact and extended) and with the ACA (7 m array plus antennae for total power measurements). An observing log of all ALMA and ACA CO(2–1) observations of NGC 5044, including the cycle 0 observation and the recent total power (TP) ALMA single-dish observation, is given in Table 1. The last row in Table 1 indicates the usage of each data set in this paper. Note that the detailed analysis of the cycle 4 12 m array data will be presented in a subsequent paper. However, we list here the cycle 4 12 m array observations for completeness. Only the highest resolution cycle 4 observations are used for the absorption study in Section 3.6. Details about the ALMA cycle 0 observation can be found in David et al. (2014). The two ALMA observations taken in cycle 4 were mosaics of 11 pointings with a Nyquist sampling covering a region of approximately 60" by 60" centered on NGC 5044. The 7 m observation was a single pointing centered on NGC 5044 and covering a region of about 40" diameter. The TP observation covers a region of about 55" × 55" scanned in raster mode. Figure 1 shows the range of

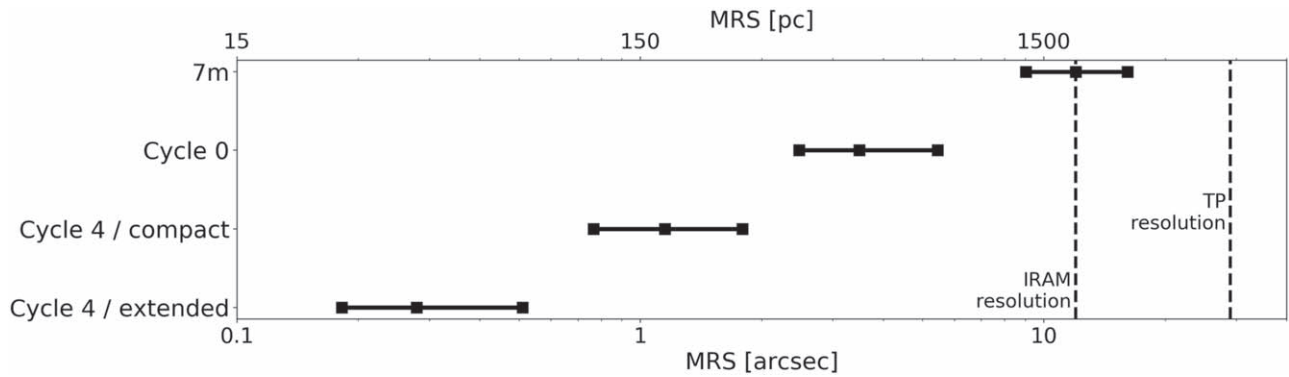


Figure 1. The three points along each horizontal line are maximum recoverable scales (MRS) that correspond to the 25%, 50%, and 75% percentiles in the cumulative baseline distribution for each array configuration. Angular scales are shown at the bottom and physical scales in the rest frame of NGC 5044 at the top. Nearly complete coverage of all angular scales is provided by the different ALMA/ACA array configurations.

angular and physical scales sampled by the ACA and ALMA for the different array configurations. As can be seen in this figure, the combination of all ALMA and ACA observations provides a nearly complete census of the total molecular mass and the detection of individual molecular clouds in NGC 5044 on scales up to the TP field of view. We use the 7 m array data for comparisons between the ALMA and IRAM measurements, showing that the total single-dish flux is recovered in the interferometer observations (e.g., Figures 2 and 5). We also use the 7 m array image cubes for the cloud detection to have slightly higher spatial resolution. We combine the 7 m array data with the total power array (7 m + TP = ACA) to measure the total CO emission at larger radii ($>12''$), where the 7 m array sensitivity drops. In the following we describe the processing steps beyond the standard pipeline.

2.1. 7 m Array

All ACA and ALMA observations were configured to provide four spectral windows within Band 6, each with a bandwidth of 185 MHz. One of the spectral windows was centered on the CO(2–1) line at 228.397 GHz. The central frequencies for the other three spectral windows were 226.418 GHz, 242.314 GHz, and 244.244 GHz. The correlator configuration was similar for all cycle 4 observations.

The 7 m data were calibrated with CASA version 4.7.2 (McMullin et al. 2007) using the ALMA pipeline scripts, but CASA version 5.4.0 was used for the subsequent imaging. Several phase self-calibration steps improved the noise level of the continuum image by a factor of 2.7, and the final solutions were applied to the spectral window containing the CO(2–1) emission. Continuum subtraction was performed with the CASA tool `uvcontsub` using the emission in the line-free regions. The CASA tool `tclean` was used to generate data cubes from the continuum-subtracted measurement set. Unless otherwise noted, we used a Briggs weighting with a robust parameter of 1, and the `multiscale` deconvolution (Cornwell 2008, with scales set to 0 and 3). For the iterative `clean` algorithm we applied the `auto-multithresh` masking algorithm with the `noisethreshold` = 4.5, and `sidelobethreshold` = 1.25, to clean until a threshold of 0.3σ is reached. The synthesized beams and the root mean square (rms) sensitivities in 10 km s^{-1} velocity channels are shown in Table 1 for all data sets, although we focus here on the ACA data.

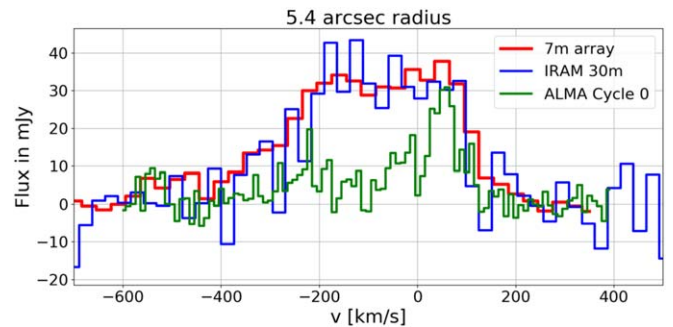


Figure 2. Comparison of IRAM 30 m (blue), 7 m array (red), and ALMA 12 m cycle 0 (green) CO(2–1) spectra. All ALMA spectra are extracted within a $5''.4$ radius aperture (i.e., the IRAM 30 m PB). The 7 m observation recovers all the flux measured by the IRAM single-dish telescope.

2.2. Total Power Array

The TP array data were recorded in nine schedule blocks in 2018 between October and December, out of which six were recorded using four antennae, two blocks with three antennae, and one block with two antennae. The science spectral window contains 2048 channels over a 2 GHz bandwidth. We used CASA version 5.4.0 to apply the pipeline calibration and flagging of bad data. On-off single-dish calibration was used to measure T_{sys} , and NGC 5044 was scanned in raster mode.

Imaging was achieved through the CASA task `sdimaging` with a spheroidal gridding function and 10 km s^{-1} channel width. We ran the pipeline task `hsc_baseline` to subtract the baseline inferred through position switching. The baseline is not flat due to spatial and spectral variability in the response. After creating an image cube, we used `imcontsub` on the line-free channels to fully subtract continuum emission.

In order to combine the 7 m and TP array image cubes, we regridded the TP image cube to match the 7 m dimensions, and divided by the 7 m primary beam (PB) to have a common PB attenuation. After combining the image cubes with the CASA task `feather`, we corrected the resulting image cube for the 7 m PB.

3. ACA Results

The primary objective of our ACA 7 m array observation was to recover the CO(2–1) emission that was resolved out in our earlier ALMA observation, but detected in the single-dish IRAM 30 m observation. A comparison between the IRAM 30 m, ALMA cycle 0, and 7 m spectra is shown in Figure 2.

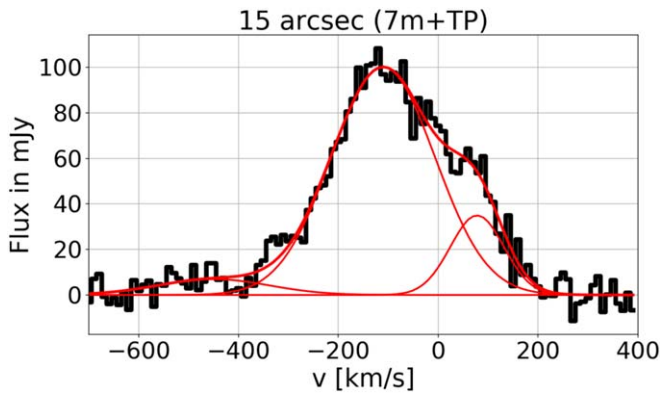


Figure 3. ALMA 7 m plus TP array spectrum (combined through feathering) within 15'' radius aperture (black). The three-Gaussian components are shown in red, and the values are given in Table 2. The spectrum is well characterized by the sum of the three broad Gaussians.

For this purpose, we also reprocessed the cycle 0 data with the latest calibration pipeline, and performed a phase self-calibration, which improved the noise level by a factor of 1.4.

The 7 m array and ALMA spectra were extracted from circular apertures with a 6'' radius (i.e., the IRAM 30 m PB). This comparison shows that essentially all of the CO(2–1) emission is recovered in the 7 m observation, indicating that the bulk of the CO(2–1) emission in NGC 5044 arises from diffuse molecular structures with spatial scales of above 1 kpc. The 7 m observation also detects significant CO(2–1) emission beyond the IRAM 30 m PB (see Figures 3 and 6), with a total extent of approximately 30''.

Figure 3 shows that the ACA CO(2–1) spectrum within 15'' radius is well represented by the sum of three broad Gaussians (also see Table 2). Note that the signal-to-noise ratios (S/N) in Table 2 reflect the integrated signal within the full width at half-maximum (FWHM) and the noise in the combined bins of the FWHM of each Gaussian component. The redshifted complex was the most massive structure detected in the ALMA cycle 0 data, and it was identified as GMC 18 by David et al. (2014). While the blueshifted molecular complex centered at -110 km s^{-1} is the most massive of the three complexes, it was almost entirely resolved out in the ALMA cycle 0 observation. The more sensitive ACA observation also detects a blueshifted molecular complex at approximately -450 km s^{-1} that almost exceeds the adiabatic sound speed of the hot gas ($c_a = 460 \text{ km s}^{-1}$). We use a likelihood-ratio analysis to verify the significance of this third component at high (negative) velocity. We find that the null hypothesis (the spectrum is described by only two Gaussians) is rejected by $p_0 < 10^{-4}$ when compared to a three component fit. This is even more significant when we use a smaller aperture (10 instead of 15 arcsec.).

3.1. Moments of the CO(2–1) Emission

In this section we investigate the large-scale properties of the molecular emission in NGC 5044 through the CO moment maps, before we compare the various total molecular mass estimates in Section 3.2, and study the emission in the individual channel maps in Section 3.3.

We generated zeroth- (integrated flux density), first- (velocity), and second-moment (velocity dispersion) maps (see Figure 4) by integrating the CO(2–1) emission between -550 and 300 km s^{-1} . The first- and second-moment maps only

Table 2
Three-Gaussian Fit to ACA Spectrum

v_0 (km s^{-1})	FWHM (km s^{-1})	Amp (mJy)	$S_{\text{CO}} \sigma$ (Jy km s^{-1})	M_{mol} ($10^7 M_{\odot}$)	S/N
-450 ± 58	263 ± 132	7 ± 2	1.8 ± 0.9	0.6 ± 0.3	5
-110 ± 5	244 ± 19	100 ± 2	26.0 ± 1.9	8.2 ± 0.6	67
-78 ± 8	126 ± 18	35 ± 6	4.7 ± 1.3	1.5 ± 0.4	16

Note. Velocity centroid, FWHM, amplitude, integrated CO(2–1) flux density, and molecular mass for the three-Gaussian fit to the ACA (7m+TP) spectrum extracted within a 15'' radius aperture (as shown in Figure 3). The total molecular mass is $10.3 \pm 0.2 \times 10^7 M_{\odot}$.

include pixels with a $S/N \geq 5$, while the zeroth-moment map includes all pixels above $S/N = 1$. We also masked out regions where the primary beam response of the 7 m telescopes drops below 50%. Due to the moderate ACA beam, the only deviation from spherically symmetric emission in the zeroth-moment map is a slight extension toward the southwest (see also velocities -160 to -80 km s^{-1} in Figure 6). The peak of the CO(2–1) emission is coincident with the location of the AGN.

A large-scale velocity gradient is evident in the first-moment map (Figure 4) along an east–west direction, with the most highly blueshifted emission located toward the southwest (i.e., the extended feature seen in the zeroth-moment map in Figure 4). Most of the redshifted emission resides in two structures: a structure toward the southeast (coincident with cloud 18 in David et al. 2014), and a fainter structure toward the northwest. The second-moment map (Figure 4) shows that the velocity dispersion of the CO(2–1) emission increases from 10 km s^{-1} at large radii to up to 140 km s^{-1} near the AGN, but this is mostly a projection effect because the emission near the AGN is summed over many individual molecular structures along the line of sight. At large radii, there are probably only a few individual molecular structures along the line of sight, and the second-moment map shows that the velocity dispersion of these structures is lower than 20 km s^{-1} .

3.2. Total Molecular Mass

The molecular mass was computed assuming the Galactic conversion factor from Bolatto et al. (2013),

$$X_{\text{CO}} = 2 \times 10^{20} \text{ cm}^{-2} (\text{K km s}^{-1})^{-1}, \quad (1)$$

which gives

$$M_{\text{mol}} = 1.05 \times 10^4 \frac{S_{\text{CO}} \Delta v}{\text{Jy km s}^{-1}} \left(\frac{D_L}{\text{Mpc}} \right)^2 (1+z)^{-1} M_{\odot}, \quad (2)$$

where $S_{\text{CO}} \Delta v$ is the integrated CO (1 – 0) flux density and D_L is the luminosity distance. As in David et al. (2014) we assume a CO(2–1) to CO(1 – 0) flux density ratio of 3.2. We note that Equation (2) includes the contribution of molecular hydrogen and helium, while all other molecules (including CO) are negligible in terms of mass. While X_{CO} is known to depend on a number of factors (e.g., metallicity and other environmental factors), the only measurement of X_{CO} appropriate for molecular gas that has condensed out of a cooling flow was done by Vantyghem et al. (2017) by observing both ^{13}CO and ^{12}CO in RXJ0821+0752. Their results suggest that the molecular mass computed assuming a Galactic X_{CO} may

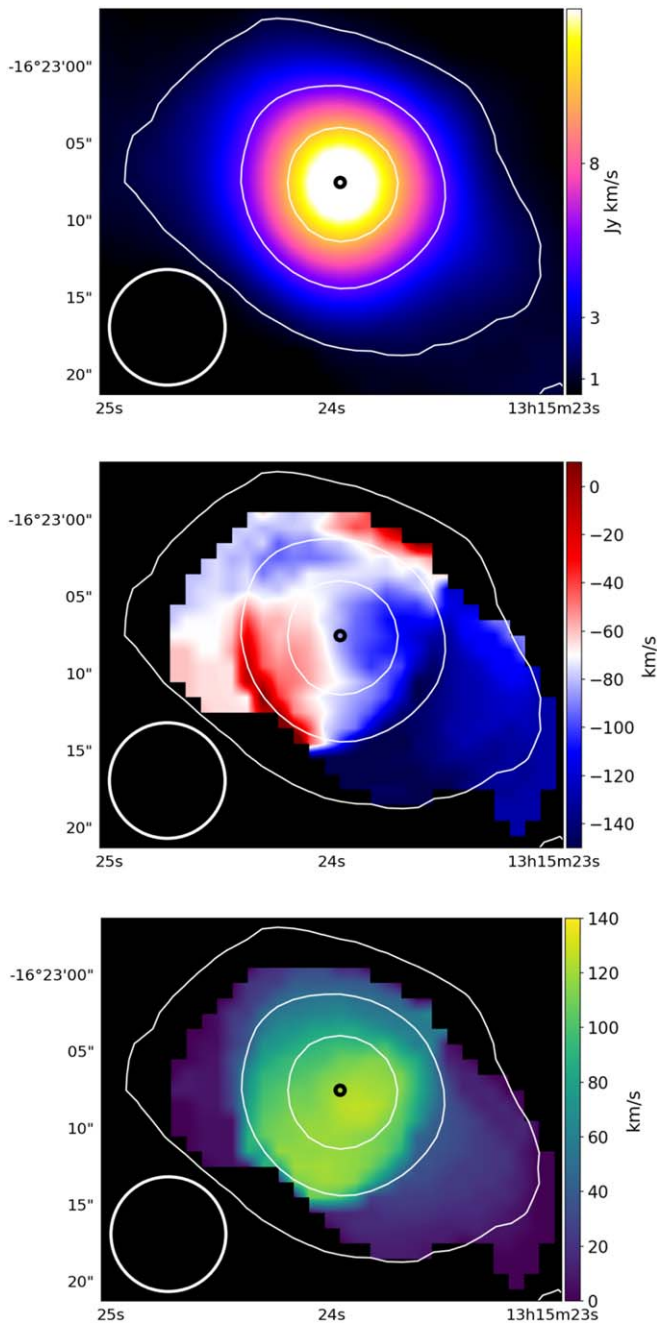


Figure 4. Zeroth (flux, top), first (velocity, middle), and second (dispersion, bottom) moments of the ACA CO(2–1) emission between -550 and 300 km s^{-1} . The first and second moments only include pixels with S/N greater than 5. White contours show the 3, 12, and 24σ levels of the zeroth-moment map. The black circle in the center shows the location of the central AGN. The most redshifted emission is oriented along the diagonal northeast-southwest axis.

overestimate the true mass by a factor of two. Lim et al. (2017) also pointed out that the physical conditions of the molecular gas in cluster or group central galaxies are likely very different from those of giant molecular clouds in our Galaxy, raising concerns about using the same X_{CO} for both. Nevertheless, to provide a simple comparison with past work as well as across different group or cluster central galaxies, we apply the factor in Equation (2).

We computed the total molecular mass within a $15''$ radius aperture (a physical radius of 2.3 kpc) using three methods: (1)

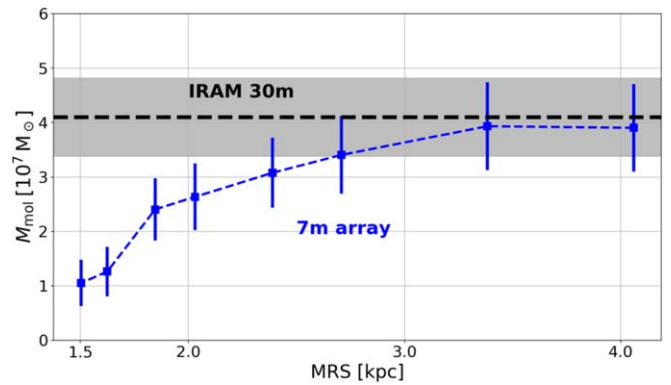


Figure 5. Total molecular mass as a function of the maximum resolvable scale (MRS) of the ACA 7 m array CO(2–1) spectra extracted from images generated with different filtering on the smallest baseline. All spectra are extracted from within $6''$ radius apertures. The total IRAM signal is recovered from molecular clouds with scales below 3.5 kpc.

from the three-Gaussian fits shown in Figure 3, (2) from the zeroth-moment image shown in Figure 4, and (3) a masked-moment map (Dame 2011). These methods yield total molecular masses of $10.3 \pm 0.2 \times 10^7 M_{\odot}$, $9.5 \pm 1.2 \times 10^7 M_{\odot}$, and $10.0 \pm 0.1 \times 10^7 M_{\odot}$, respectively, which are in relatively good agreement.

In addition to determining the concentration of the molecular gas toward the center of NGC 5044, we also computed the total molecular mass within the $6''$ radius aperture (a physical radius of 0.9 kpc) shown in Figure 2 and obtained a (projected) mass of $4.2 \pm 0.1 \times 10^7 M_{\odot}$. For comparison, the deprojected (i.e., spherical) mass of the hot X-ray emitting gas within 0.75 and 1.5 kpc is $1.1 \times 10^7 M_{\odot}$ and $5.6 \times 10^7 M_{\odot}$, respectively. Thus, the molecular gas is more centrally concentrated than the hot gas and dominates the total gas mass within the central kiloparsec.

Interferometry enables us to test the spatial scales on which the CO emission is distributed: We filter the data on different uv scales to exclude the largest scales, and derive the mass only from smaller physical scales. The dependence shown in Figure 5 illustrates that most of the emission comes from scales of 2 kpc, and the maximum size is 3 kpc. Between 2 and 3 kpc, the molecular mass is doubled.

3.3. ACA Channel Maps

A set of 16 channel maps from ACA (7 m + TP) is shown in Figure 6. Molecular structures are detected in all velocity bins between -560 and 230 km s^{-1} . Due to the large ACA beam, most of the structures are only marginally resolved, but there are clearly two separate structures in the -100 km s^{-1} velocity bin. The highly blueshifted structure is clearly detected in the -560 to -440 km s^{-1} velocity bin, just $2''.5$ to the north of the AGN. This velocity is about two times higher than the stellar velocity dispersion (see David et al. 2009), and could be related to uplift of material by the AGN. An infalling cloud with $\sim 500 \text{ km s}^{-1}$ line-of-sight velocity has to be very close to the AGN to reach this velocity. However, the projected distance (375 pc) as a lower limit for the distance to the AGN excludes the possibility of an infalling cloud.

All of the blueshifted CO(2–1) emission between -200 km s^{-1} and 0 was resolved out in our higher resolution cycle 0 observation (David et al. 2014). CO(2–1) emission can only arise from the cores of GMCs where the densities are

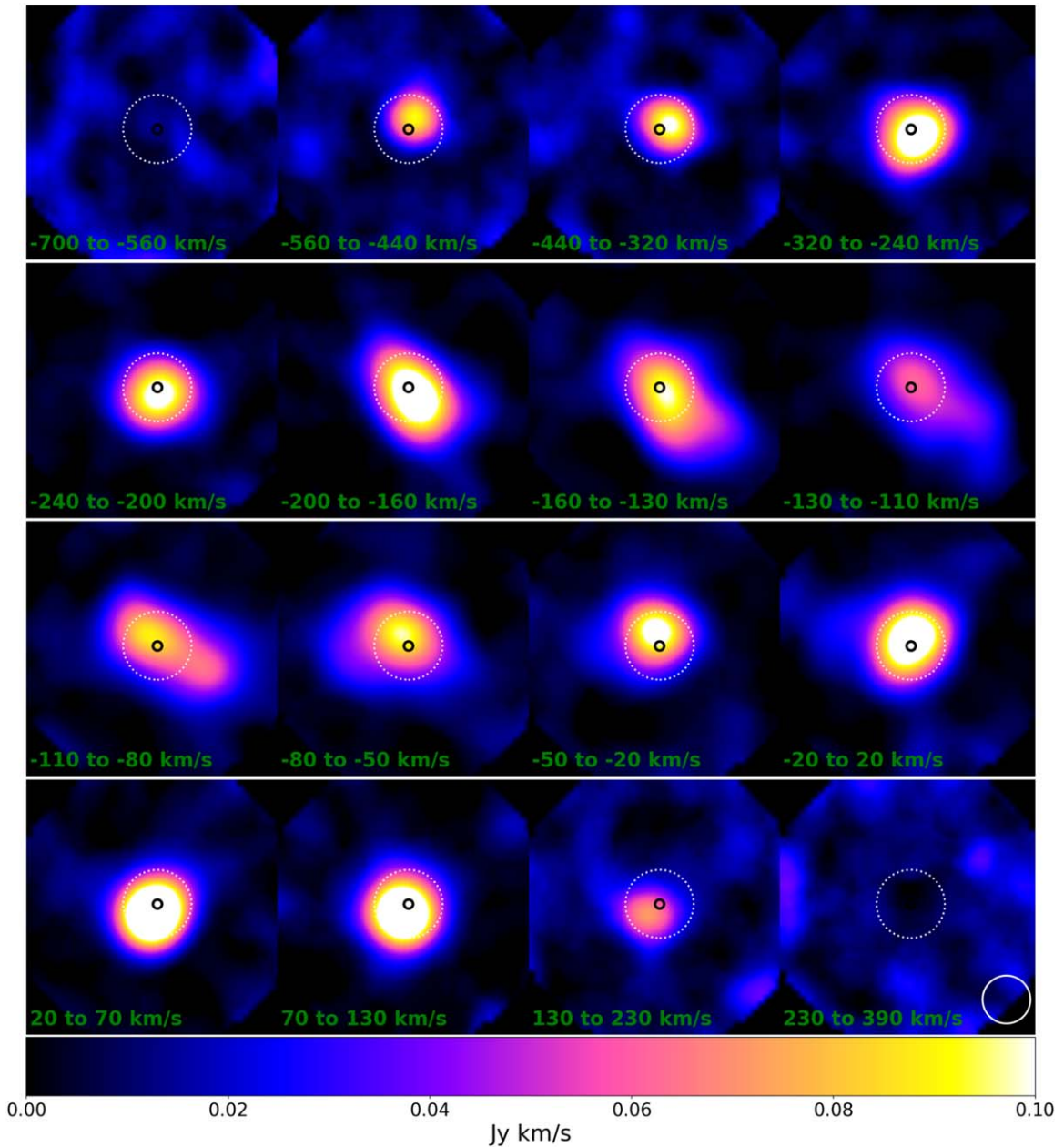


Figure 6. Zeroth-moment maps of the ACA data cubes, binned to have the same integrated flux in each velocity bin. The black circle marks the position of the continuum source, while the white dotted circle marks the 6'' (900 pc) radius of IRAM. Each image is about 40'' across. We find extended emission (clearly outside the IRAM beam) between -200 and -50 km s^{-1} . The ACA beam size is shown in the lower right corner.

comparable to the critical H_2 density of 10^4 cm^{-3} . All of the structures shown in Figure 6 have a very low volume filling factor of molecular gas, with most of the volume filled with hot, X-ray emitting gas.

These results show that long baselines detect molecular structures with high GMC volume filling factors, or equivalently, regions where the GMCs are strongly clustered, and short baselines detect emission from molecular structures with low GMC volume filling factors, or where the GMCs are widely separated. Our results show that for nearby systems such as NGC 5044, a broad range of baselines is required to determine the complete census of the molecular content.

The 7 m array data combined with the TP observations allow us to measure the CO emission out to 20'' radius, which is close to the TP field of view. Figure 7 shows the total molecular mass

inferred from the integrated CO(2–1) signal as a function of radius. We see no significant increase in emission beyond 15'' radius.

3.4. Molecular Cloud Properties

In order to identify individual clouds from the ACA signal, we used the CLUMPFIND algorithm (Williams et al. 1994). We use the ACA 7 m array datacube with a 10 km s^{-1} velocity binning. We tested the detection algorithm with several velocity binnings from 2 to 50 km s^{-1} . The very fine binning of 2 km s^{-1} yields a large number of clouds, most of them just in a single or two velocity bins, and thus not useful for us to derive further properties. The difference between 5 km s^{-1} and 10 km s^{-1} is small (nine versus eight clouds). A binning of 20 km s^{-1} and larger results in only a few clouds, which are not

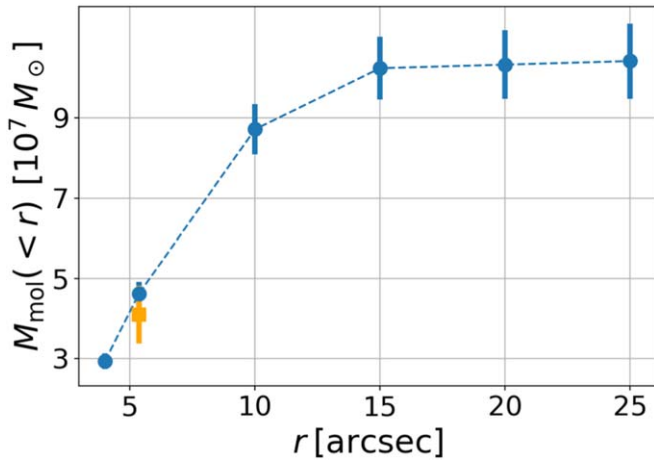


Figure 7. ACA cumulative molecular mass profiles (blue dots). The orange square represents the IRAM measurement. We see no CO(2–1) emission outside 1.5 kpc radius ($10''$).

well sampled by the velocity resolution. The 3D locations of the three largest clouds in the 20 km s^{-1} image cube are similar to the detections in the 10 km s^{-1} cube. The optimal binning should be a compromise between a slight oversampling of clouds in velocity space and still having good sensitivity in the individual binned channels. When we assume an ideal oversampling in velocity space of a factor of 2 to 5 with respect to the cloud FWHM, we find that all the detected clouds are best covered by the 10 km s^{-1} binning, which will be our default for the cloud detection.

To know how many false detections are expected in our sample of clouds, we inverted the image cube (by multiplying with -1), and reran the detection algorithm on the new image cube, which should contain noise and possible absorption lines in the positive values. From this test we find two clouds (at 255 and 265 km s^{-1}), which turn out to be real absorption features; we discuss this in more detail in Section 3.6. We do not find any false detection.

Following Pineda et al. (2009), we adopt the optimal threshold and stepsize parameters for CLUMPFIND, 5σ and 3σ , respectively, which results in eight detected clouds (see Table 3; Figures A1, A2, and A3 show the moment maps for all except the smallest cloud). The 5σ threshold makes false detections from noise unlikely. Note that we also list the unidentified emission, i.e., everything outside the clouds, as ID 0. In contrast to the S/N of features in the spectrum (as in Tables 2 and 5), the S/N of clouds (Table 3) is the peak flux value of a cloud divided by the rms, which reflects the definition of them_{CLUMPFIND} threshold parameter. The velocity width of cloud ID 8 cannot be determined because almost all pixels belonging to this clump were found in one single channel. The summed masses of the individual clouds (ID 1–8), which are almost entirely within $8''$, is $5 \times 10^7 M_{\odot}$. This is about 70% of the total molecular mass within a radius of $8''$. The location and mass of cloud ID 1 are in relatively good agreement with clouds 18 and 19 from David et al. (2014) using only the 12 m cycle 0 ALMA data. This cloud would have to consist of clumps below 600 pc size in order to be fully detected in the cycle 0 data. Other individual clouds from David et al. (2014) cannot be found in the 7 m data because of the spatial resolution of the ACA data and low fluxes of these clouds, i.e., the flux density sensitivity is too low in the ACA data.

Table 3
Cloud Properties

ID	$\langle v \rangle$ (km s^{-1})	σ (km s^{-1})	M_{mol} ($10^7 M_{\odot}$)	r ($''$)	S/N
1	-60 ± 5	21 ± 10	1.16 ± 0.12	2.2	19
2	-31 ± 15	21 ± 8	1.19 ± 0.11	2.0	15
3	-172 ± 7	10 ± 6	0.74 ± 0.06	2.8	13
4	-109 ± 12	16 ± 9	0.81 ± 0.08	1.4	12
5	-216 ± 6	10 ± 6	0.53 ± 0.05	2.0	12
6	-124 ± 10	10 ± 7	0.37 ± 0.04	7.6	10
7	-269 ± 12	16 ± 15	0.24 ± 0.04	2.2	8
8	-542 ± 4	<5	<0.01	2.2	5
0	-174 ± 153	277 ± 96	3.34 ± 0.18	1.0	

Note. Velocity centroid, velocity dispersion, molecular mass, and projected distance from the continuum source of the detected clouds. ID0 corresponds to all emission that is not included in detected clouds.

Table 4
Comparison between Cycle 0 and ACA-detected Clouds

ACA Cloud ID (1)	Cycle 0 Cloud ID (2)	CO $\langle v \rangle$ (km s^{-1}) (3)	f_{CO} (%) (4)
1	18	59	87
2	13	-38	28
3	6, 7, 8	-160	80
4	9	-113	10
5	2,3,4	-230	89
6	10	-132	25

Note. Columns are the detected cloud in the ACA data (1), see also Table 3), the corresponding cloud detections in the cycle 0 data (2), from David et al. (2014), the average velocity (3) and the fraction of the ACA cloud mass found in corresponding cycle 0 clouds (4).

We also create individual moment maps (zeroth, first, and second moment) for each cloud by only selecting the pixels of the image cube assigned to a cloud by CLUMPFIND (shown in Figures A2 and A3). For this we extended slightly (by a few arcseconds) the identification in the spatial dimensions to avoid sharp cutoffs. Clouds ID 2 and 5 show signs of rotation in the first-moment map, while ID 6 seems to have an irregular, noncircular shape. The bottom panel of Figure A3 shows moments of the unclassified emission (everything except detected clouds), which generally appears as a ring around the central regions where most clouds are detected. This is likely a selection effect because clouds at larger projected distances are usually not as bright, and the instrumental sensitivity is reduced. We investigate the possibility of rotating clouds in Section 4.3.

3.5. Comparison with Clouds in ALMA Cycle 0 Data

We detect 8 molecular gas clouds in our ACA data set with the CLUMPFIND algorithm. The cycle 0 data set of the ALMA 12 m array (about six times higher spatial resolution, see Table 1) has been analyzed by David et al. (2014), who detected 24 clouds. Although the two data sets are sensitive to clouds on different spatial scales, we can make a comparison between the detected clouds (see Table 4).

David et al. (2014) found 11 clouds in the cycle 0 data that are located at a large offset angle from the continuum source. We exclude these clouds from the following considerations

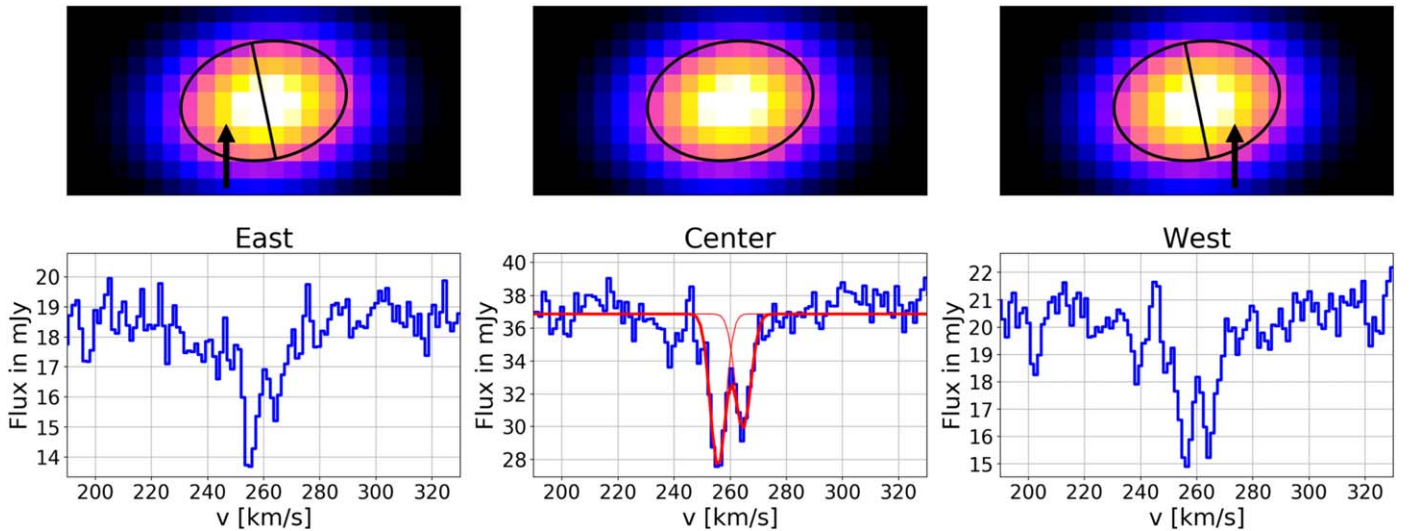


Figure 8. Spectrum of the central continuum source highlighting the two strong, redshifted absorption features at $v = 255$ and 265 km s^{-1} . The feature at higher redshift is strongest in the western part of the continuum source. In the center panel, the aperture is centered on the continuum source and has the extent of the beam, while in the other two cases, the eastern or western half is excluded. The spatial dependence of the absorption feature indicates that the continuum source is only slightly smaller than the point-spread function.

because the noise level at large offset angles (2.5 kpc) is about three times higher than in the phase center of the same observation. This can lead to false detections by the CLUMPFIND algorithm.

Two clouds from the cycle 0 data could not be clearly identified in the ACA image cube (cycle 0 ID 11 and 15), although they are located very close to the center. Cycle 0 cloud ID 15 has the lowest mass of all the detected clouds ($3 \times 10^5 M_\odot$), so it is likely below the detection threshold of the ACA data. Cloud 11 has a high molecular mass ($4 \times 10^6 M_\odot$), but also a very broad velocity distribution, causing the flux in the 10 km s^{-1} channels to be below the ACA sensitivity (which is lower than the cycle 0 threshold).

We also calculate for each ACA-detected cloud the fraction of molecular mass that was detected as a cycle 0 cloud (Column 4 in Table 4). As seen already in the spectrum (Figure 2), the fluxes of ACA clouds 1, 3, and 5 have been almost entirely captured by the cycle 0 observation, while the other clouds are more extended and cannot be fully detected by the ALMA 12 m array.

3.6. Absorption Features in the AGN Spectrum

In Section 3.4 we noted the detection of two absorption features with respect to the emission of the AGN in the inverted (negative) image cube. We analyze the ALMA cycle 4 extended array data (see Table 1) with superior spatial resolution to characterize the nature of this absorption feature.

We detect two absorption features at a velocity of $\sim 260 \text{ km s}^{-1}$ in the continuum-subtracted CO(2–1) spectrum (Figure 8 shows the absorption in the continuum spectrum for three apertures) at the location of the central continuum source (AGN). The proximity of the absorption features to the AGN, at least as seen in projection, can be estimated from the extent of the 230 GHz continuum emission. We note that David et al. (2014) detected one absorption line in the continuum spectrum of the ALMA cycle 0 data of NGC 5044 with a velocity of 260 km s^{-1} , and a line width of 5.2 km s^{-1} .

To obtain the best spatial resolution, we imaged the 12 m cycle 4 extended array observation using a Briggs robust parameter of -2 , selecting only baselines longer than $1000 \text{ k}\lambda$, and a velocity bin of 2000 km s^{-1} (to maximize the S/N). This produced a restoring beam of $0''.08$ by $0''.05$, which corresponds to a geometric mean radius of 5 pc. Using the CASA task `imfit`, we found that the resulting 0th moment image of the AGN continuum emission at 230 GHz is consistent with that of a point source.

The absorption features can be modeled by Gaussians, for which best-fit values are given in Table 5. As for the emission spectrum (Table 2), the S/N values reported here are integrated within the FWHM. Following Rose et al. (2019b), we can derive the molecular hydrogen column density of the absorbing clouds from the optical depth profile, τ_{ul} ,

$$N_{\text{tot}} = Q(T_{\text{ex}}) \frac{8\pi\nu_{ul}^3}{c^3} \frac{g_l}{g_u} \frac{1}{A_{ul}} \frac{1}{1 - e^{-h\nu_{ul}/kT_{\text{ex}}}} \int \tau_{ul} d\nu. \quad (3)$$

$Q = 15.52$ is the partition function for a given excitation temperature, T_{ex} (we assume 42 K, as derived by Rose et al. 2019b for Hydra A), $g_l = 3$ and $g_u = 5$ are the degeneracies of the lower and upper level, $A_{ul} = 6.914 \times 10^{-7}$ is the Einstein coefficient, and $\nu_{ul} = 230.538 \text{ GHz}$ is the frequency of the CO(2–1) transition. For the absorption features in NGC 5044, we obtain a CO column density of $2.2 \times 10^{17} \text{ cm}^{-2}$, which converts into a H₂ column density of $N_{\text{H}_2} = 1.5 \times 10^{20} \text{ cm}^{-2}$ (Sofia et al. 2004). This assumes a surface filling factor of 1, and the column density will be higher when the cloud does not fill the whole source. Looking at all the ALMA observations between 2012 and 2018, we do not detect any significant change in the absorbing column density.

We note that the amplitude of the second absorption line (centered at 265 km s^{-1}) varies slightly with position, mainly along the east–west direction. This is illustrated in Figure 8 by the absorption spectra in three apertures along the east–west line. The amplitude of the second absorption line in the eastern half is about three times above the spectral noise level, while in

Table 5
Gaussian Fits to the AGN Absorption Features

Velocity (km s ⁻¹)	FWHM (km s ⁻¹)	Amplitude (mJy)	Mass (10 ³ M _⊙)	Radius (pc)	S/N
255.5 ± 0.3	6.6 ± 0.3	9.5 ± 0.8	7	4	15
264.7 ± 0.4	6.3 ± 0.4	7.2 ± 0.8	6	4	9

Note. The two-Gaussian fits to the 12 m spectrum extracted within an aperture representing the beam size (center in Figure 8). Masses and radii have been estimated from the line width, assuming the velocity-radius relation, and that the system is in virial equilibrium.

all other cases the absorption lines are at least five times above the noise.

With the release of CASA 5.5.0¹¹ the `perchanweight-density` parameter was introduced for the `tclean` task. It allows the calculation of the Briggs weighting scheme on a per-channel-base for image cubes. Changes are predominantly small, but the second absorption line in the eastern half of the continuum source changes: Setting this parameter to `True` increases the amplitude of this line, erasing any significant differences between the two absorption lines in the western or eastern half of the continuum source. Without deeper high-resolution data, we are unfortunately unable to confirm the existence of a spatially variable absorption feature.

4. Discussion

4.1. Gas Cooling

Werner et al. (2014) detected [C II] emission to a radius of 8 kpc, which is associated with atomic or nuclear material (because NGC 5044 lacks significant star formation, see Werner et al. 2014). We detect molecular CO(2–1) emission out to about 2 kpc (the TP observations are sensitive to more than 3 kpc), while it is possible that a more extended component of CO is hidden below our detection threshold. When we assume a connection between the atomic and molecular gas components, a more extended molecular component at a level comparable to the rms in the 0th moment maps and with a uniform extent over $8 \times 8 \text{ kpc}^2$ can increase the total molecular mass to $\sim 10^8 M_{\odot}$.

4.1.1. Feedback Models

In contrast to Bondi accretion, the chaotic cold accretion (CCA) model (e.g., Gaspari et al. 2013; Voit et al. 2015a; Tremblay et al. 2016; Gaspari et al. 2017) predicts the condensation of cold clouds out of the turbulent atmosphere. These clouds will eventually “rain” on the supermassive black hole (SMBH) and trigger feedback.

The simulations for the CCA model (Gaspari et al. 2018) include hydrodynamics, cooling, heating, and, most importantly, turbulence at subparsec resolution. Predictions include small clouds with high line-of-sight velocities and low velocity dispersions (thus larger volume filling factors $\sim 2\%$) close to the SMBH. Molecular gas with smaller line-of-sight velocities and higher dispersions are located at larger distances to the central AGN. In any case, turbulent pressure is key to prevent clouds from collapsing. Any significant turbulence will also prevent high star formation rates.

Prior studies using deep high-resolution X-ray data have shown that the hot gas within the central region of NGC 5044 has been perturbed by at least three cycles of AGN outbursts and the motion of the central galaxy within the group potential. Cavities at various distances from the AGN have been related to the oldest outburst (Giacintucci et al. 2011), intermediate outbursts (David et al. 2009), and the most recent AGN activity cycle (David et al. 2017). The mechanical heating by AGN-inflated cavities is sufficient to offset radiative cooling of the gas within the central 10 kpc.

A contrasting feedback description by McNamara et al. (2016) claims that feedback from the AGN is stimulated through buoyantly rising cavities that lift low-entropy gas, with molecular clouds forming in the wakes of the uplifted cavities (“updraft model”). Significant turbulence should exist in the wakes of the rising bubbles, leading to density fluctuations and cooling, as discussed by Gaspari et al. (2013). Brighenti et al. (2015) suggest that those cavities trigger episodes of enhanced cooling. As shown in Figure 9, the cavities (red) are aligned in NW–SE direction, while the H α filaments and the CO are elongated perpendicular to this axis. The updraft model makes a clear link between the cold molecular gas and the rising bubbles, and one would expect a spatial correlation between the two.

4.1.2. H α in NGC 5044

To draw a link between the cavities and cold gas, we have to take into account the distribution of warm line-emitting ionized gas in NGC 5044 traced by H α emission. NGC 5044 was observed with MUSE in four nights from 2015 January 17 to 2015 February 3, for seven exposures of 820 s each (PI: Hamer). MUSE provides a spectroscopic datacube on a rectangular $1' \times 1'$ field, with a spectral coverage of (4800–9000) Å. The MUSE data were reduced using the v2.6.2 ESO MUSE pipeline within the Zurich Atmosphere Purge software (Soto et al. 2016). More details on the MUSE data reduction will be given in a subsequent paper (M. Sun et al. 2020, in preparation).

Here, we include the MUSE H α image (Figure 9) and the central velocity map (Figure 10) to compare with the ALMA data.

We find an S-shape distribution in H α observations. Within the central 3 kpc, the cold CO-emitting gas is aligned well with the H α filaments along a NE–SW axis (white and black dashed contours in Figure 9). Resolved CO clouds (Temi et al. 2018) in the center are aligned along the same axis, while some clouds are located at the outer edge of the H α filaments (filled white circles in Figure 9). At larger distances, we do not detect CO emission, and the H α filaments are bent toward the N–S direction. The cavities are distributed along a NW–SE axis (red ellipses in Figure 9), which seems to be uncorrelated with the CO emission. We note that an intermediate-distance cavity in the south is located between the H α filaments, and seems to be partly surrounded by it. This could be an indication that there is a connection between the cavities and the H α filaments. However, we also see molecular clouds in other region of the central part of the galaxy, unrelated to cavities. Based on our finding, we cannot exclude either the CCA or the updraft model for the feedback processes in NGC 5044.

The velocity structure of the H α filaments shown in Figure 10 shows a trend of blueshifted gas to the NW and redshifted emission to the SE. In the central 2 kpc (Figure 10), we find some similarities between the CO and the H α

¹¹ <https://casa.nrao.edu/casadocs/casa-5.5.0/introduction/release-notes-550>

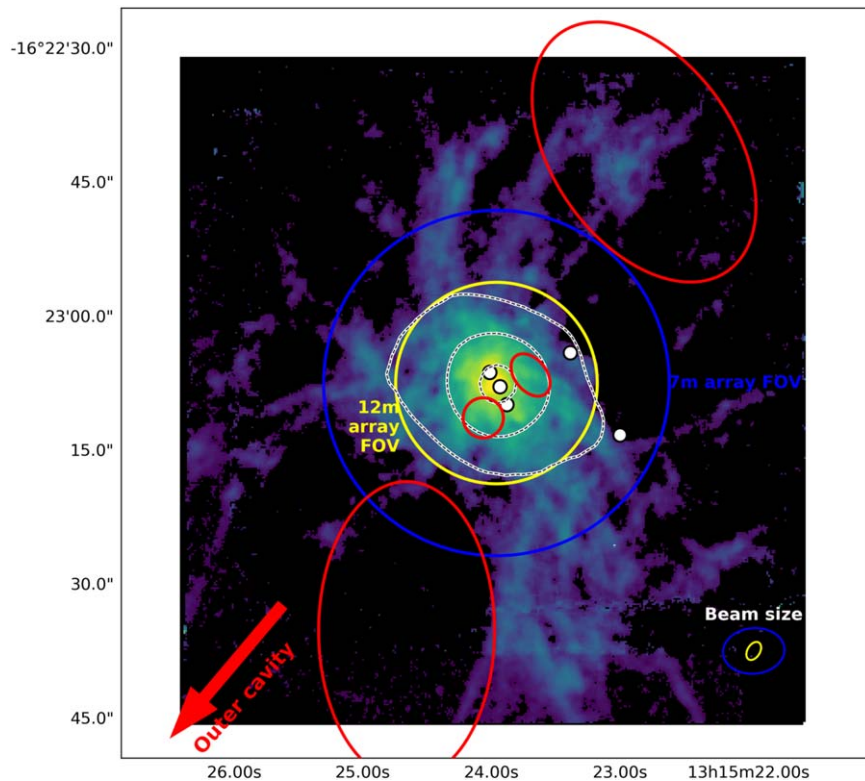


Figure 9. MUSE H α image (M. Sun et al. 2020, in preparation) of NGC 5044 with CO contours. White and black dashed contours show the detected CO emission from ACA. Red ellipses indicate the detected cavities in the X-ray image (David et al. 2017), and white filled circles mark the locations of the resolved CO clouds in the ALMA cycle 0 data (Temi et al. 2018). The major axis orientation of the CO emission is roughly consistent with the H α filament. Blue and yellow circles and ellipses show the 7 m and 12 m array FOVs and beam sizes.

filamental velocity structure, although the resolution of the two maps is very different.

4.1.3. Comparing the Molecular Clouds in NGC 5044 with CCA Model Predictions

Simulations of the CCA model predict molecular gas to be in a certain location of the velocity shift—velocity dispersion diagram (Figure 11). These two quantities trace the kinematics of molecular structures depending on the detection aperture. Either one traces an ensemble in a larger aperture excluding the nuclear region (blue ellipse in the top left of Figure 11) or a small “pencil-beam” aperture through the center of the AGN (green ellipse in the center of Figure 11). The ensemble region comprises a larger amount of condensed gas at larger distances from the AGN, while the pencil beam typically picks up single small (low-velocity dispersion) clouds with large line-of-sight velocity components close to the AGN.

All emission and absorption data points (blue and red crosses and squares in Figure 11) are detected features in the CO spectra. Only orange stars in Figure 11 show identified clouds. We find that the ACA-detected clouds (orange stars, Table 3) are within the expected range of the pencil-beam detections, while the expected range for ensemble-beam detections (single spectrum approach) is shifted to higher velocity dispersion and smaller velocity offset.

We also overplot the CO emission found by Rose et al. (2019a) for a few nearby objects ($z < 0.2$) detected from the CO spectrum (dark red crosses), which all fall in the ensemble region. The absorption detections from Rose et al. (2019a; light blue crosses) and our absorption features (blue squares) populate the lowest part

of the plot, just within the pencil-beam detection region. The bias of these small clouds seen in absorption toward lower $\sigma_{v,los}$ could be caused by a lower level of turbulence in the hot gas.

Our ACA clouds (orange stars) are the only detections found through a cloud-detection algorithm. This explains their location in Figure 11 between the large molecular filaments detected through spectral fitting and the small clouds seen in absorption. Our detection for NGC 5044 from the ACA spectrum (in this case, using only a single Gaussian to be consistent with the ensemble assumption, shown as a red square in Figure 11) is shifted to higher velocity dispersions, consistent with the CCA ensemble prediction (blue ellipse). In summary, we find consistent results with the predictions of the CCA model. However, our CLUMPFIND-detected clouds in the ACA data fill the gap (in the velocity dispersion—line-of-sight velocity phase space) between larger ensembles and small individual clouds found in absorption.

4.2. Total Amount of Molecular Gas

The hot-gas temperature within the central 15" (2.3 kpc) in NGC 5044 is about 0.8 keV. We adapt the power-law model of the hot-gas density distribution from Equation (2) in David et al. (2017) to derive the hot-gas mass within 1.5 kpc of $3 \times 10^7 M_{\odot}$, which is about 50% of the molecular mass within the same radius. The molecular gas in NGC 5044 is about an order of magnitude lower than that found in the Perseus cluster (Lim et al. 2008; Salomé et al. 2008). Other galaxy groups have been found to host more molecular gas than NGC 5044 (O’Sullivan et al. 2018), likely due to a merger, but NGC 5044 contains more molecular gas than any other cooling-flow

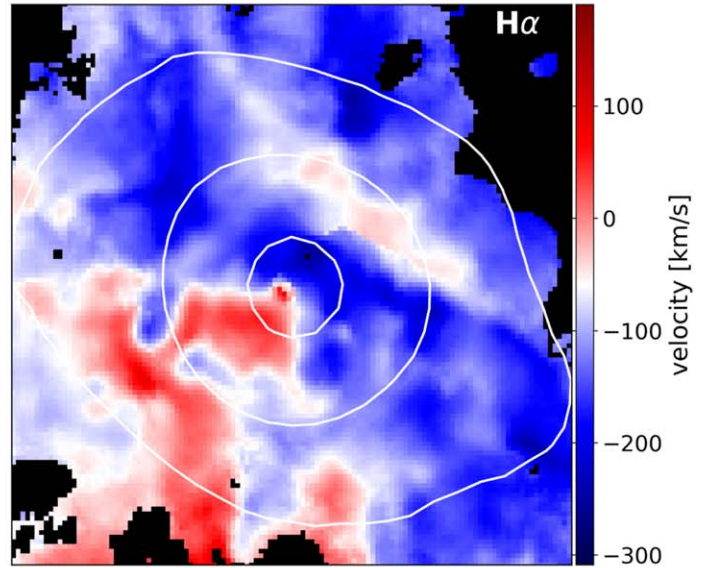
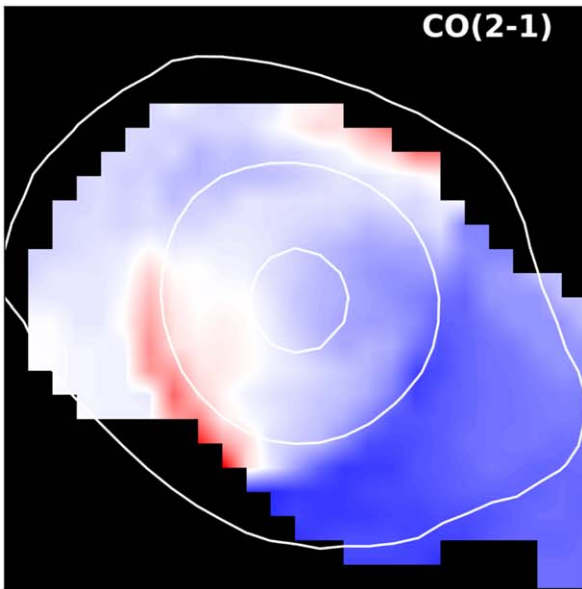


Figure 10. CO (2–1) velocity map close up (left, as in Figure 4), and MUSE H α first-moment map (M. Sun et al. 2020, in preparation) of NGC 5044 with CO contours (right). The image size is 24'' (3.6 kpc).

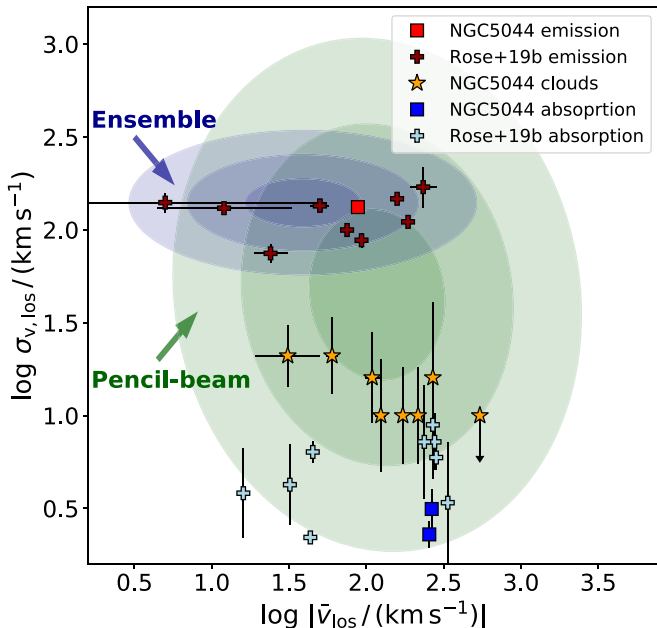


Figure 11. Comparison of observations with the CCA model (Gaspari et al. 2018). The blue shaded region shows single spectrum and ensemble predictions, while the green shaded ellipse is associated with pencil-beam detections in simulations. Data points show observational detections: CO emission in red, CO absorption in blue, and detected clouds in orange.

group we know of (i.e., a combination of a short central cooling time and an X-ray bright cool core). A possible explanation for this is that the AGN in NGC 5044 is currently not in an active phase, and the galaxy group has not experienced recent mergers, allowing the formation of molecular gas through the cooling processes in the center. The gas-depletion timescale for the molecular gas in NGC 5044 is at least 800 Myr, given the current upper limit for the star formation rate estimated from a combination of far-UV (FUV) and mid-IR (MIR) data ($0.073 M_{\odot} \text{ yr}^{-1}$, Werner et al. 2014), which is in agreement with central dominant

galaxies in galaxy groups (O’Sullivan et al. 2018). However, the duty cycle of the outbursts in NGC 5044 is about 10^8 yr, so that most of the molecular mass will be reheated.

4.3. Cloud Properties

4.3.1. Virial Equilibrium in Detected Clouds

Knowing the sizes of the newly detected molecular clouds is important to derive other quantities. We applied the CASA task `imfit` to the zeroth-moment maps of the individual clouds to measure the extent (beam deconvolved) from our ACA data. We can derive (beam-deconvolved) sizes for clouds 1 to 5, where we define the size as the square root of the product of the two fitted FWHM along the major and minor axis. We find 308 ± 22 pc, 684 ± 10 pc, 717 ± 16 pc, 538 ± 24 pc, and 541 ± 21 pc for the first five clouds, all with axis ratios around 2, except for cloud 2, which is almost circular. The other clouds are not resolved. Together with the cloud mass, M , and the velocity dispersion, σ_v (both given in Table 3), we can test whether virial equilibrium is established using the expression for the virial parameter α (Bertoldi & McKee 1992),

$$\alpha = \frac{5R\sigma_v^2}{GM}, \quad (4)$$

which gives the ratio of kinetic and gravitational energy. Perfect virial equilibrium is established for $\alpha = 1$. For the five resolved clouds, we find α of typically around 8. Because of the large uncertainties of the cloud velocity dispersions, these values are also very uncertain. However, we can derive an average, $\alpha = 8.6 \pm 3.4$. The ACA-detected clouds are much closer to bound structures than smaller clouds detected in cycle 0 data by Temi et al. (2018), which have α ranging from 30 to 650 (250 on average). Because of its shorter baselines, the 7 m array is able to detect large-scale emission (see Figure 1), which traces the size of the clouds more accurately. However, even values of $\alpha = 8$ are at the upper end of what has been found by simulations of molecular clouds in the Milky Way

(Dobbs et al. 2011), and those clouds are still considered globally unbound. The dispersion timescale, $\frac{r}{\sigma_v}$, is on the order of a few million years (up to 35 Myr), which sets an upper limit for the lifetime of the clouds.

For two of the clouds (IDs 2 and 5), we find rotational characteristics in the first-moment maps, from which we estimate maximum velocity difference within each cloud by eye to be on the order of 20–40 km s⁻¹. This can be used to derive a dynamical mass, if we assume rotational support. However, the typical timescale for one rotation is several times above the dispersion timescale. Therefore we do not assume that the clouds are actually globally in rotation, but consist of smaller subclouds in motion. The combination of the 7 m array data with the higher resolution 12 m array will enable us to resolve the clouds better and measure the average density and the radius. We will present this in a subsequent paper.

4.4. Molecular Clouds in Absorption

The spectrum of the central AGN, which is visible in the continuum image as a point source, shows two clouds in absorption (Figure 8). The two clouds must reside within a projected distance of 5 pc to the AGN (resolution of the continuum image). For comparison, the sphere of influence of the central black hole,

$$R_a = GM_{\text{bh}}/\sigma_*^2 \approx 17 \text{ pc}, \quad (5)$$

where $M_{\text{bh}} = 2.3 \times 10^8 M_\odot$ and $\sigma_* = 237 \text{ km s}^{-1}$, is more than three times larger than the upper limit of the projected distance of the two clouds from the black hole. If the infalling clouds are actually located within the sphere of influence of the black hole, they will eventually likely be accreted.

4.4.1. Absorbing Cloud Properties

As described in Tremblay et al. (2016), we can calculate the mass of an absorbing molecular cloud from the line width assuming virial equilibrium,

$$M_{\text{cloud}} \approx \frac{R_{\text{cloud}} \sigma^2}{G}. \quad (6)$$

For the two absorption line features at 255 and 265 km s⁻¹, we determine masses of about 6×10^3 – $7 \times 10^3 M_\odot$ (see Table 5). The expected size can be derived from the scaling relation by Solomon et al. (1987),

$$\sigma = (1.0 \pm 0.1) \times S^{0.50 \pm 0.05} \text{ km s}^{-1}, \quad (7)$$

where the size S is given in parsec. With Equation (7), we find a cloud size of roughly a factor of 2 smaller than the observed (unresolved) upper limit on the central continuum source extent (5 pc radius). From the integrated absorption signal, we can estimate the H₂ column density of the absorbing material to be roughly $2.3 \times 10^{21} \text{ cm}^{-2}$. Given the estimated mass and size of the cloud, we obtain a density of 400 cm^{-3} , which is comparable to that of a giant molecular cloud. The line widths and densities of the clouds along the line of sight result in a turbulent pressure of about $\frac{P}{k_B} = 1.9 \times 10^6 \text{ K cm}^{-3}$, which is in agreement with the hot-gas pressure of $\sim 2 \times 10^6 \text{ K cm}^{-3}$ (David et al. 2014). However, cloud mass and size estimates are based on scaling relations, so it is hard to conclude if the absorbing clouds are really in pressure equilibrium with the

surrounding gas. Following the argument by Field et al. (2011), the external pressure of the hot gas implies a maximum mass of the molecular cloud under the assumption of a stable equilibrium. For the absorbing clouds in NGC 5044, this maximum mass is about 30 times higher than the derived masses from Equation (6).

4.4.2. Distance to the AGN

Tremblay et al. (2016) found CO absorption in A 2597, and inferred that the absorbing material location was close to the central black hole of A 2597 (about 1 kpc in projection). The authors also find at a similar velocity HI absorption from a VLBA observation (resolution about 20 pc). In NGC 5044 we find CO absorption at a projected distance of less than 5 pc. If the real separation of the absorbing clouds from the AGN is close to the projected distance, we have detected molecular clouds much closer to the AGN than previously observed in a cooling-flow system.

In the following we try to derive the real separation of the absorbing clouds from the AGN. Brüggén & Scannapieco (2016) show that various timescales have to be considered when estimating the lifetime of a molecular cloud in the environment of X-ray bright gas. The time after which a cloud is destroyed by a shock induced through the motion within the intracluster medium (ICM) is the cloud crushing timescale,

$$t_{\text{cc}} = \left(\frac{T_{\text{ext}}}{T_{\text{cloud}}} \right)^{0.5} \frac{R_c}{v_h} \approx 7 \text{ Myr}, \quad (8)$$

where $T_{\text{cloud}} \approx 10 \text{ K}$ (Braine & Combes 1992) and $T_{\text{ext}} \approx 0.8 \text{ keV } k_B^{-1}$ (David et al. 2017) are the cloud and surrounding gas temperatures, respectively, $R_c \approx 2 \text{ pc}$ is the cloud radius, and $v_h = 260 \text{ km s}^{-1}$ is the velocity of the cloud. Thermal conduction will heat up the cold cloud within the evaporation time,

$$t_{\text{evap}} = \frac{R_c}{v_h} \frac{100}{f(M)} \approx 0.8 \text{ Myr}, \quad (9)$$

where $f(M) = 1$. This timescale is a lower limit and can be longer in the presence of magnetic fields. Cooling of the cloud through radiation would also decrease this timescale, but is not considered here. The third timescale to be considered is the Kelvin–Helmholtz instability timescale,

$$t_{\text{KH}} \approx 5 \frac{R_c}{v_h} \left[1 + 4(\gamma - 1) \frac{v_h}{c_{\text{sc}}} \right]^{0.5} \approx 240 \text{ Myr}, \quad (10)$$

where $\gamma = \frac{7}{5}$ is the adiabatic index for CO, and $c_{\text{sc}} \approx 6.6 \times 10^{-2} \text{ km s}^{-1}$ is the sound speed in the cloud. We conclude that the infalling cloud should last for at least 400 kyr if it is not destroyed by cloud–cloud collisions.

Given the lifetime of the cloud, we can calculate how close the cloud is to the AGN when a relative velocity of 260 km s^{-1} is reached, assuming that only gravity accelerates the cloud toward the SMBH. As shown in Figure 12, a cloud falling from a distance of 350 pc (85 pc, 10 pc) will reach our threshold velocity at a distance of 27 pc (22 pc, 8 pc) after 7 Myr (800 kyr, 21 kyr). When we take the evaporation timescale as our threshold for the cloud lifetime, we conclude that the cloud is 22 pc or closer to the SMBH. This is very close to the sphere of influence of the SMBH (17 pc, see Equation (5)). When we

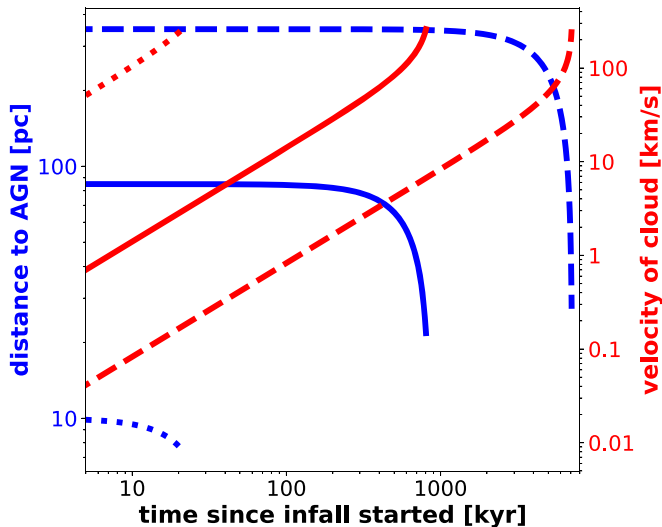


Figure 12. Infall simulation showing velocity (red) and distance of the cloud to the AGN (blue) as a function of time. The different linestyles refer to initial distances of the cloud (350 pc: dashed, 85 pc: solid, 10 pc: dotted). For each initial distance the cloud reaches the observed velocity (260 km s^{-1}) after a different time (350 pc: 7 Myr, 85 pc: 800 kyr, and 10 pc: 21 kyr), and at a different (final) distance to the AGN (350 pc: 27 pc, 85 pc: 22 pc, and 10 pc: 8 pc).

assume a uniform distribution of clouds, there is a $\frac{17 \text{ pc}}{22 \text{ pc}} \approx 80\%$ chance that the two clouds are within the sphere of influence of the black hole. Given all our assumptions (clouds with mass $10^4 M_{\odot}$ initially at rest, falling within the thermal conduction time), this means that the absorbing clouds in NGC 5044 are closer to the black hole than the clouds in A 2597, but they are also orders of magnitude smaller.

We note that in the scenario described above, we assume a cloud falling onto the SMBH through gravity alone. However, in the CCA model (see Section 4.1.3), clouds share the same velocity as the hot gas until they dynamically separate from the hot gas after some time, and leaving less time for the cloud to fall toward the SMBH.

4.4.3. Spatial Variability of the AGN Absorption Features

The NGC 5044 continuum source (AGN) is variable on timescales of years at millimeter wavelengths (Alastair Edge, private communication), implying an upper limit on the size of at least one component of the source of $\sim 1 \text{ pc}$. With our four ALMA and ACA observations (between 2012 and 2018), we estimate a linear decline of the continuum source flux at 229 GHz of -1.6 mJy yr^{-1} . Our ALMA CO(2–1) observations also allow us to place limits on the spatial extent of the AGN: At 244 GHz (highest frequency spectral window), the beam size is $70 \times 40 \text{ mas}$ ($10.5 \times 6 \text{ pc}$). Even with this small beam, the continuum source appears to be unresolved. The CASA task `imfit` is able to deconvolve the source and places constraints on the physical extent ($10 \times 7 \text{ mas}$, or $1.5 \times 1.0 \text{ pc}$, with 10% and 90% relative 1σ uncertainties along the major and minor axis, respectively).

The absorption features in the spectrum of the continuum source suggest spatial variability (see Section 3.6), which cannot be confirmed with an alternative analysis mode. Deeper observations are needed to confidently confirm the weakened second absorption line in the western half of the continuum source.

If the variability feature is real, we suggest two scenarios: (1) the CO emission of a cloud on the eastern side of the absorbing

cloud partially covers the continuum source and fills (compensates for) the absorption, and (2) the continuum source is extended near the ALMA resolution, and two different clouds cover two parts of the continuum source (e.g., core and jet). For scenario (1), additional CO(2–1) emission is needed to fill in the absorption line on the eastern side of the core, where the 265 km s^{-1} absorption line is less visible. The flux of this absorbed line would correspond to the emission of a cloud of $\sim 1.4 \times 10^5 M_{\odot}$. However, we can also estimate the mass from the line width of the absorbing cloud, assuming virial equilibrium, which results in a mass 50 times lower than the “required” mass, if emission compensates the absorption feature on one side. We also do not see any other signs of CO(2–1) emission in the continuum spectrum of the source, and scenario (1) is likely ruled out.

For scenario (2), we estimated the feasibility with a basic simulation of two spatially separated continuum sources, each having an absorption feature at a different velocity (see Figure 13, left panel). These two sources could represent a core and a jet. However, active jet spectra are typically steeper than the core spectra, which can make them hard to be detected at millimeter wavelengths. By smoothing the image cube spatially with a Gaussian about three times the separation of the two emitting continuum sources, we obtain an image that is consistent with a point source at the ALMA resolution (Figure 13, right panel), which shows a very similar spatial dependence of the absorption as in NGC 5044.

From the variability of the continuum source flux (on timescales of years), the unresolved nature of the point source at the highest frequency being not perfectly consistent with the beam shape, and the possibility of spatial variability of the absorption features, we have indications that the continuum source in NGC 5044 has a physical extent of a factor of a few below the ALMA resolution (15 pc).

4.4.4. Feedback Energy

NGC 5044 has the largest known reservoir of cold molecular gas of any dominant galaxy in a cooling-flow group, and three epochs of AGN activity are visible as cavities in its hot gas (David et al. 2009; Giacintucci et al. 2011; David et al. 2017). In Section 4.4.2 we concluded that the two molecular clouds visible as absorption features in the spectrum of the continuum source are most likely within the sphere of influence of the AGN. We can now estimate the energy input to the AGN by those infalling clouds.

Within 800 kyr, two clouds of total mass $1.3 \times 10^4 M_{\odot}$ might fall onto the SMBH, which gives a mass-accretion rate for this line of sight of $0.016 M_{\odot} \text{ yr}^{-1}$. The possible feedback energy from the infalling cloud, assuming mass - energy equivalence, is about $1.2 \times 10^{56} \text{ erg}$, assuming a 50% accretion efficiency and that 1% of the available energy is turned into radiation or powering the jet. This will be a lower limit for the accretion rate because a shorter infall is possible. If the cloud is located at the sphere of influence, it covers a solid angle of about 80 deg^2 , as seen from the location of the black hole. When we integrate over the whole sphere, the total mass-accretion rate is $6 M_{\odot} \text{ yr}^{-1}$, which is far above any typical mass-accretion rate for central dominant galaxies, and it is about 550 times the Bondi accretion rate. This is an upper limit in case clouds are distributed everywhere around the SMBH.

For a distance close to the AGN ($\sim 5 \text{ pc}$) and a line-of-sight velocity (260 km s^{-1}), the freefall timescale is about 140 kyr,

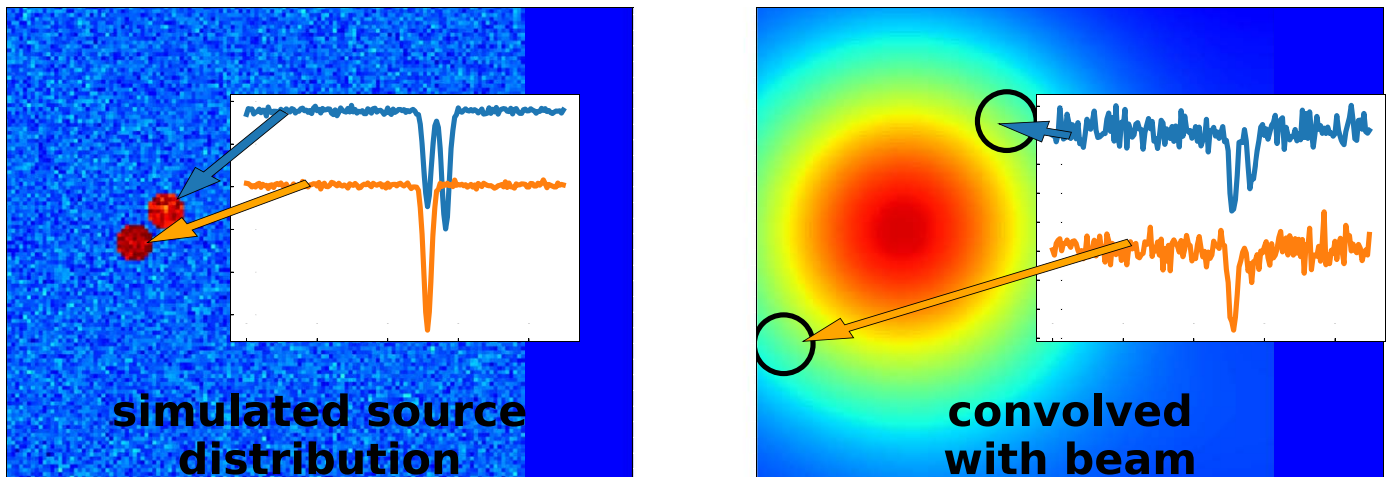


Figure 13. Left: hypothetical distribution of two sources (red circles) with different spectra (shown in orange and blue). Right: after convolution with a larger Gaussian, only one point source is visible, but the spatial variability of the absorption spectrum (tested at two different points, as shown by the black circles) is similar to our observations of NGC 5044.

which implies a mass-deposition rate of $\sim 0.09 M_{\odot} \text{ yr}^{-1}$. The energy rate (assuming again a radiative efficiency of 0.5%) is $2.6 \times 10^{43} \text{ erg s}^{-1}$, which is several orders of magnitude higher than the bolometric X-ray or integrated radio luminosity of the AGN, and also twice higher than the total cavity power (southern cavity plus smaller northern cavities, see David et al. 2009), which is related to several AGN outbursts in the past. This implies that more than half of each infalling cloud does not reach the AGN.

In the literature we find comparable galaxy groups in a similar dynamical state as NGC 5044, having a centrally peaked, relaxed X-ray morphology with a short central cooling time (Hudson et al. 2010; Voit et al. 2015b; O’Sullivan et al. 2017). However, examples such as NGC 4636 and NGC 5846 show much less cold molecular gas than NGC 5044. The radio power at GHz frequencies of NGC 5044 is about an order of magnitude higher than these two galaxies, which should indicate stronger feedback, preventing the formation of cold gas (O’Sullivan et al. 2018). Moreover, the cavity power and star formation rate are highest for NGC 5044 compared to NGC4636 and NGC5846. However, the cavity radio spectrum shows by far the steepest spectral index for NGC 5044 (α of 1.9 or higher, while the other two galaxies have ~ 0.65 , see O’Sullivan et al. 2011). This indicates that the visible signs of major feedback are not recent for NGC 5044, while the other two galaxies had more recent outbursts of the AGN. We note that other cavities in NGC 5044 reported by David et al. (2009, 2017) appear to be related to more recent AGN outbursts, but are much smaller than the outburst with the steep radio spectrum. NGC 5044 may thus have had longer to replenish its CO reservoir since the last major AGN outburst.

5. Summary

We report the analysis of the ALMA 12 m extended array data and the ACA (7 m plus total power array) CO(2–1) data for the central dominant galaxy of the nearby galaxy group NGC 5044. David et al. (2014) found molecular gas in this galaxy, accumulated in clouds, but the total emission detected in this high-resolution interferometer observation was far below the single-dish measurement. This discrepancy motivated the additional observation of NGC 5044 with ACA to cover short baselines. Our results can be summarized as follows:

1. ACA detects all of the emission that was missed by the 12 m ALMA observation, and the ACA measurement is consistent with the IRAM single-dish measurements. The total molecular gas mass within a circular aperture of 15'' radius is $6.5 \pm 0.2 \times 10^7 M_{\odot}$.
2. Extended emission beyond the IRAM single-dish beam size of 6'' radius is detected in the SW-NE direction with relative velocities of -100 km s^{-1} . The velocity range of the total CO(2–1) emission ranges from -550 to 230 km s^{-1} .
3. The CLUMPFIND algorithm detects 10 individual clouds in the ACA data, which account for about 70% of the total emission.
4. An absorption feature (reported in David et al. 2014) can be quantified in great detail in the high angular resolution data set. The emission from the continuum source (SMBH) features two absorption lines at 255 and 265 km s^{-1} , where the latter is strongest in the western region and is not detected in the eastern region. This means that the continuum emission region is only slightly smaller than the point-spread function. Assuming virial equilibrium, we estimate the mass of the two absorbing clouds from their line widths as a few thousand to $10^4 M_{\odot}$. The two clouds are consistent with being in pressure equilibrium with the surrounding gas.
5. In projection, the absorbing structures lie within 5 pc (the continuum image resolution) of the central source. By combining the thermal evaporation timescale with constraints from the infall velocity, we argue that the distance from the absorbing clouds to the AGN is less than 19 pc. Assuming a uniform distribution of clouds, there is a 80% chance that the absorbing clouds are located within the sphere of influence of the SMBH.

This paper makes use of the following ALMA data: 2011.0.00735.S, 2016.1.00533.S, 2016.2.00134.S, 2017.1.00784.S. ALMA is a partnership of ESO (representing its member states), NSF (USA) and NINS (Japan), together with NRC (Canada), MOST and ASIAA (Taiwan), and KASI (Republic of Korea), in cooperation with the Republic of Chile. The Joint ALMA Observatory is operated by ESO, AUI/NRAO, and NAOJ. The National Radio Astronomy Observatory is a facility of the National Science Foundation operated under cooperative agreement by

Associated Universities, Inc. Support for this work was provided by the National Aeronautics and Space Administration (NASA) through Chandra award Nos. GO6-17121X, AR9-20013X, issued by the Chandra X-ray Observatory Center (CXC), which is operated by the Smithsonian Astrophysical Observatory (SAO) for and on behalf of NASA under contract NAS8-03060. This research made use of NASA’s Astrophysical Data System Bibliographic Services and Astropy, a community-developed core Python package for astronomy. Basic research in radio astronomy at the Naval Research Laboratory is supported by 6.1 Base funding. W.F. and C.J. acknowledge support by the High Resolution Camera program of NASA contract NAS8-03060 and

the Smithsonian Astrophysical Observatory. J.L. acknowledges support from the Research Grants Council of Hong Kong through grant 17304817 for the conduct of this work. M.S. acknowledges support from the NSF grant 1714764.

Appendix CO Cloud Maps

Here we provide more detailed maps of the detected clouds in the ACA CO data. Figure A1 shows a 3D representation of the cloud locations, and Figures A2 and A3 show the zeroth, first, and second moment maps for each cloud.

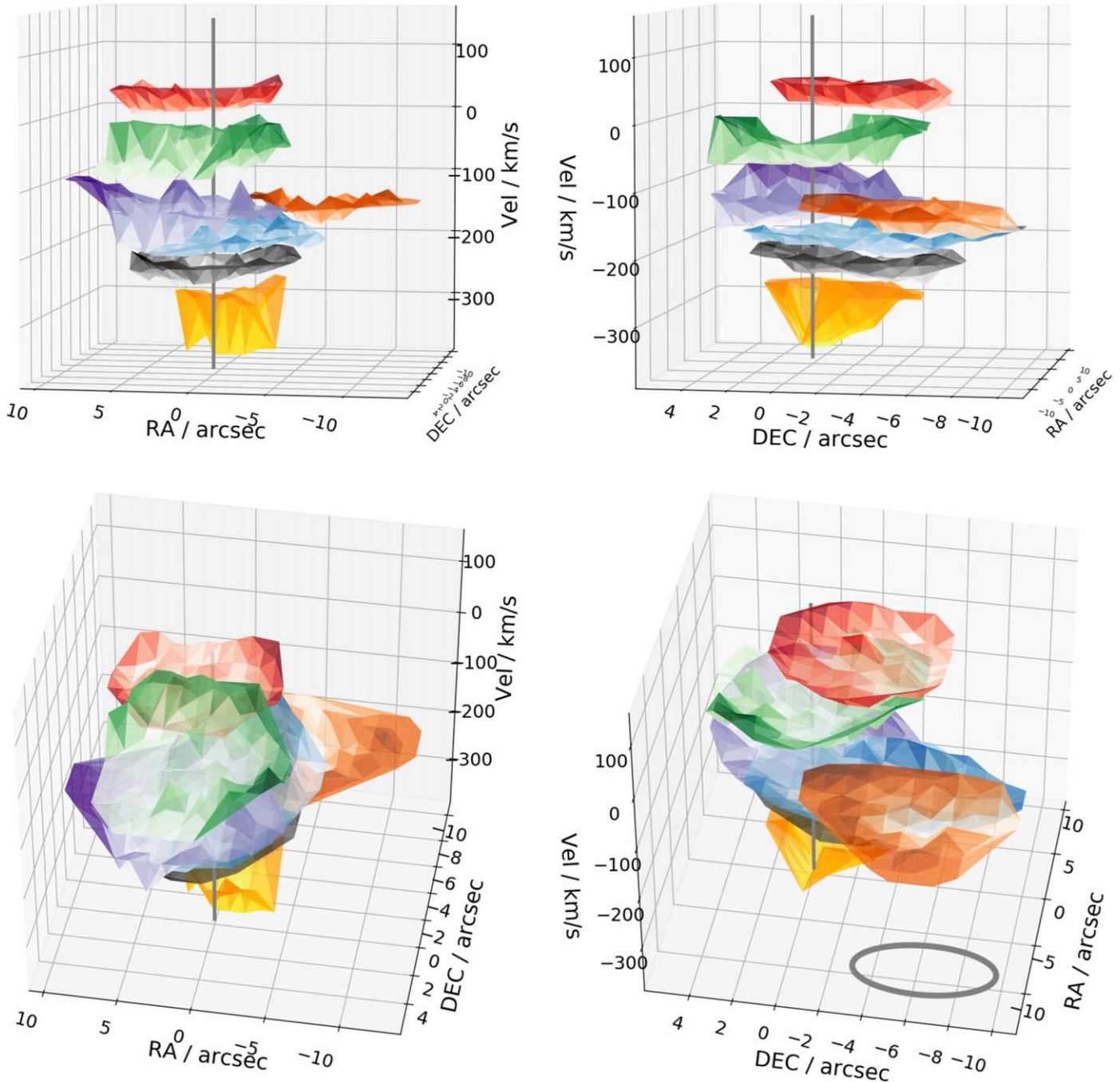


Figure A1. 3D representation of the CLUMPFIND-detected clouds in the ACA data in spatial and velocity space for different angles. The clouds overlap spatially and can only be separated in velocity space. Colors correspond to cloud IDs (defined in Table 3): 1—red, 2—green, 3—blue, 4—purple, 5—gray, 6—orange, and 7—yellow. The ellipse in the bottom right panel shows the ACA beam.

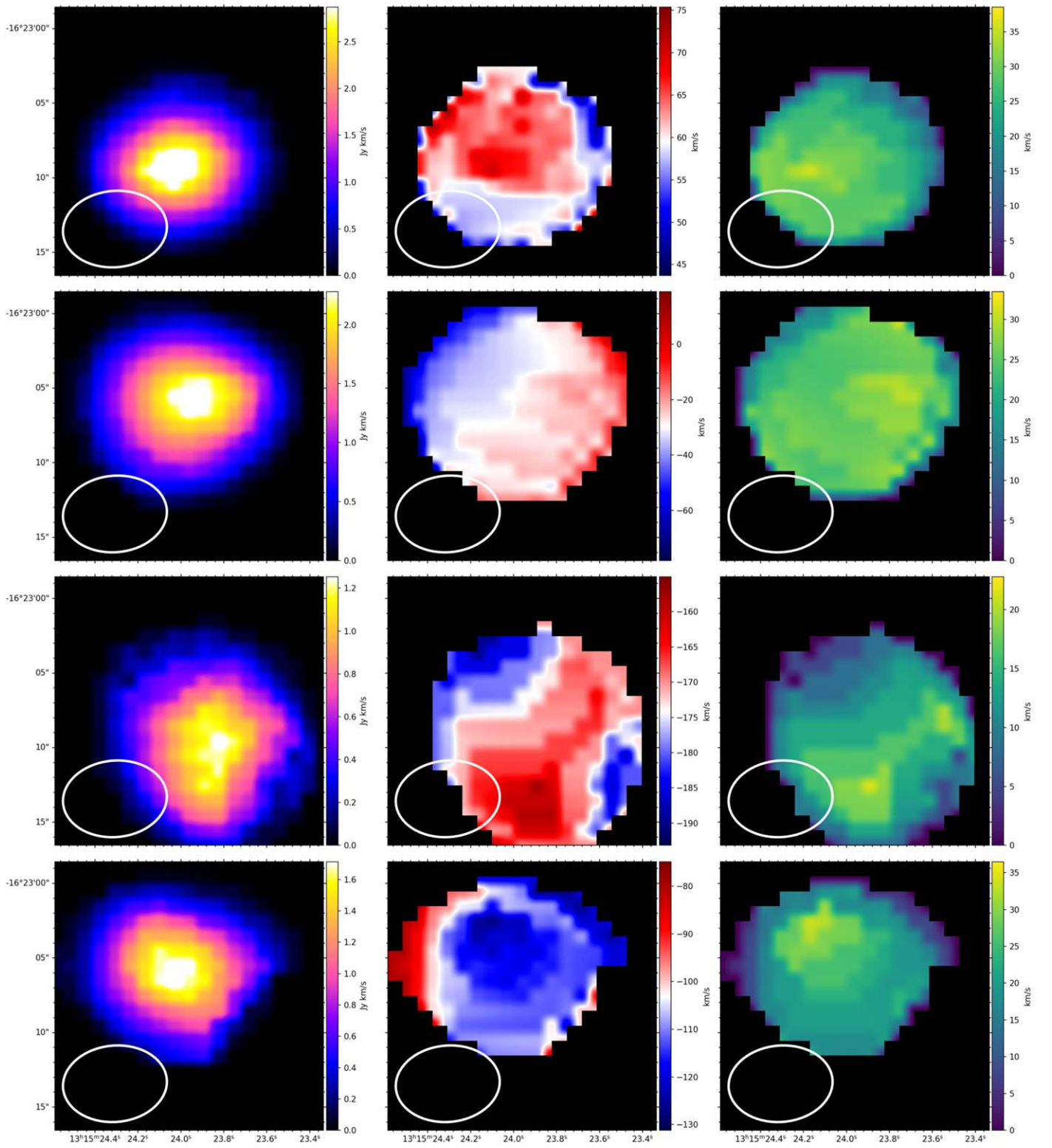


Figure A2. Zeroth- (left), first- (middle), and second-moment (right) maps of the detected clouds. From the top to the bottom row, the cloud IDs are 1 through 4 (see Table 3). The beam size is shown in the lower left corner.

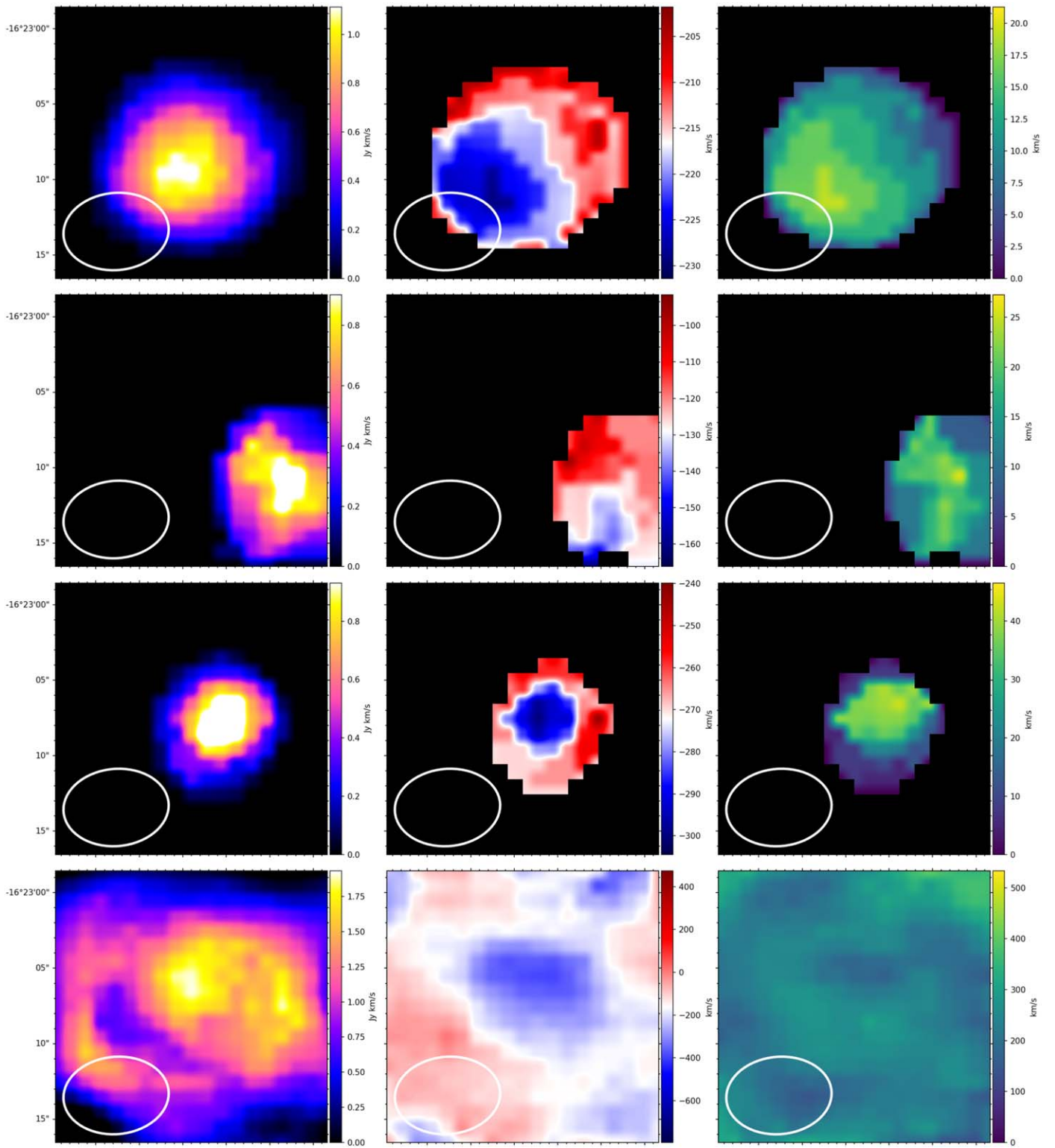




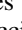








Figure A3. Zeroth- (left), first- (middle), and second-moment (right) maps of the detected clouds. From the top to the bottom row, the cloud IDs are 5, 6, 7, and 0 (see Table 3).

ORCID iDs

Gerrit Schellenberger  <https://orcid.org/0000-0002-4962-0740>
 Ewan O'Sullivan  <https://orcid.org/0000-0002-5671-6900>
 William Forman  <https://orcid.org/0000-0002-9478-1682>
 Ming Sun  <https://orcid.org/0000-0001-5880-0703>
 Françoise Combes  <https://orcid.org/0000-0003-2658-7893>
 Simona Giacintucci  <https://orcid.org/0000-0002-1634-9886>
 Alastair Edge  <https://orcid.org/0000-0002-3398-6916>
 Fabio Gastaldello  <https://orcid.org/0000-0002-9112-0184>
 Pasquale Temi  <https://orcid.org/0000-0002-8341-342X>
 Fabrizio Brighenti  <https://orcid.org/0000-0001-9807-8479>
 Sandro Bardelli  <https://orcid.org/0000-0002-8900-0298>

References

- Bertoldi, F., & McKee, C. F. 1992, *ApJ*, 395, 140
 Bolatto, A. D., Wolfire, M., & Leroy, A. K. 2013, *ARA&A*, 51, 207
 Braine, J., & Combes, F. 1992, *A&A*, 264, 433
 Brighenti, F., Mathews, W. G., & Temi, P. 2015, *ApJ*, 802, 118
 Brüggén, M., & Scannapieco, E. 2016, *ApJ*, 822, 31
 Cornwell, T. J. 2008, *ISTSP*, 2, 793
 Dame, T. M. 2011, arXiv:1101.1499
 David, L. P., Jones, C., Forman, W., et al. 2009, *ApJ*, 705, 624
 David, L. P., Lim, J., Forman, W., et al. 2014, *ApJ*, 792, 94
 David, L. P., Vrtillek, J., O'Sullivan, E., et al. 2017, *ApJ*, 842, 84
 Dobbs, C. L., Burkert, A., & Pringle, J. E. 2011, *MNRAS*, 413, 2935
 Edge, A. C. 2001, *MNRAS*, 328, 762
 Fabian, A. C. 1994, *ARA&A*, 32, 277
 Field, G. B., Blackman, E. G., & Keto, E. R. 2011, *MNRAS*, 416, 710
 Gaspari, M., McDonald, M., Hamer, S. L., et al. 2018, *ApJ*, 854, 167
 Gaspari, M., Ruszkowski, M., & Oh, S. P. 2013, *MNRAS*, 432, 3401
 Gaspari, M., Temi, P., & Brighenti, F. 2017, *MNRAS*, 466, 677
 Giacintucci, S., O'Sullivan, E., Vrtillek, J., et al. 2011, *ApJ*, 732, 95
 Hudson, D. S., Mittal, R., Reiprich, T. H., et al. 2010, *A&A*, 513, A37
 Lim, J., Ao, Y., & Trung, D. V. 2008, *ApJ*, 672, 252
 Lim, J., Trung, D. V., Vrtillek, J., David, L. P., & Forman, W. 2017, *ApJ*, 850, 31
 McMullin, J. P., Waters, B., Schiebel, D., Young, W., & Golap, K. 2007, in ASP Conf. Ser. 376, *Astronomical Data Analysis Software and Systems XVI*, ed. R. A. Shaw, F. Hill, & D. J. Bell (San Francisco, CA: ASP), 127
 McNamara, B. R., & Nulsen, P. E. J. 2007, *ARA&A*, 45, 117
 McNamara, B. R., Russell, H. R., Nulsen, P. E. J., et al. 2016, *ApJ*, 830, 79
 Olivares, V., Salomé, P., Combes, F., et al. 2019, *A&AS*, 631, A22
 O'Sullivan, E., Combes, F., Salomé, P., et al. 2018, *A&AS*, 618, A126
 O'Sullivan, E., Giacintucci, S., David, L. P., et al. 2011, *ApJ*, 735, 11
 O'Sullivan, E., Ponman, T. J., Kolokythas, K., et al. 2017, *MNRAS*, 472, 1482
 Pineda, J. E., Rosolowsky, E. W., & Goodman, A. A. 2009, *ApJL*, 699, L134
 Rose, T., Edge, A. C., Combes, F., et al. 2019a, *MNRAS*, 489, 349
 Rose, T., Edge, A. C., Combes, F., Gaspari, M., et al. 2019b, *MNRAS*, 485, 229
 Russell, H. R., McDonald, M., McNamara, B. R., et al. 2017a, *ApJ*, 836, 130
 Russell, H. R., McNamara, B. R., Edge, A. C., et al. 2014, *ApJ*, 784, 78
 Russell, H. R., McNamara, B. R., Fabian, A. C., et al. 2016, *MNRAS*, 458, 3134
 Russell, H. R., McNamara, B. R., Fabian, A. C., et al. 2017b, *MNRAS*, 472, 4024
 Salomé, P., & Combes, F. 2003, *A&AS*, 412, 657
 Salomé, P., Combes, F., Revaz, Y., et al. 2008, *A&AS*, 484, 317
 Sofia, U. J., Lauroesch, J. T., Meyer, D. M., & Cartledge, S. I. B. 2004, *ApJ*, 605, 272
 Solomon, P. M., Rivolo, A. R., Barrett, J., & Yahil, A. 1987, *ApJ*, 319, 730
 Soto, K. T., Lilly, S. J., Bacon, R., Richard, J., & Conseil, S. 2016, *MNRAS*, 458, 3210
 Temi, P., Amblard, A., Gitti, M., et al. 2018, *ApJ*, 858, 17
 Tonry, J. L., Dressler, A., Blakeslee, J. P., et al. 2001, *ApJ*, 546, 681
 Tremblay, G. R., Oonk, J. B. R., Combes, F., et al. 2016, *Natur*, 534, 218
 Vantyghem, A. N., McNamara, B. R., Edge, A. C., et al. 2017, *ApJ*, 848, 101
 Voit, G. M., Bryan, G. L., O'Shea, B. W., & Donahue, M. 2015a, *ApJL*, 808, L30
 Voit, G. M., Mark Voit, G., Donahue, M., et al. 2015b, *ApJL*, 803, L21
 Werner, N., Oonk, J. B. R., Sun, M., et al. 2014, *MNRAS*, 439, 2291
 Williams, J. P., De Geus, E. J., & Blitz, L. 1994, *ApJ*, 428, 693